



An EarthCARE/ATLID simulator to evaluate cloud description in climate models

Mathieu Reverdy, Hélène Chepfer, D. Donovan, Vincent Noël, Grégory Césana, Christophe Hoareau, Marjolaine Chiriaco, Sophie Bastin

► To cite this version:

Mathieu Reverdy, Hélène Chepfer, D. Donovan, Vincent Noël, Grégory Césana, et al.. An EarthCARE/ATLID simulator to evaluate cloud description in climate models. *Journal of Geophysical Research: Atmospheres*, 2015, 120 (21), pp.11090-11113. <10.1002/2015JD023919>. <insu-01201791>

HAL Id: insu-01201791

<https://insu.hal.science/insu-01201791v1>

Submitted on 19 Jul 2020

HAL is a multi-disciplinary open access archive for the deposit and dissemination of scientific research documents, whether they are published or not. The documents may come from teaching and research institutions in France or abroad, or from public or private research centers.

L'archive ouverte pluridisciplinaire **HAL**, est destinée au dépôt et à la diffusion de documents scientifiques de niveau recherche, publiés ou non, émanant des établissements d'enseignement et de recherche français ou étrangers, des laboratoires publics ou privés.



HAL Authorization

RESEARCH ARTICLE

10.1002/2015JD023919

Key Point:

- EarthCARE simulator to evaluate cloud in climate models

Correspondence to:

M. Reverdy,
mathieu.reverdy@lmd.polytechnique.fr

Citation:

Reverdy, M., H. Chepfer, D. Donovan, V. Noel, G. Cesana, C. Hoareau, M. Chiriaco, and S. Bastin (2015), An EarthCARE/ATLID simulator to evaluate cloud description in climate models, *J. Geophys. Res. Atmos.*, 120, 11,090–11,113, doi:10.1002/2015JD023919.

Received 21 JUL 2015

Accepted 11 SEP 2015

Accepted article online 16 SEP 2015

Published online 10 NOV 2015

An EarthCARE/ATLID simulator to evaluate cloud description in climate models

M. Reverdy¹, H. Chepfer², D. Donovan³, V. Noel¹, G. Cesana², C. Hoareau¹, M. Chiriaco⁴, and S. Bastin⁴
¹LMD/IPSL, CNRS, Ecole Polytechnique, Palaiseau, France, ²LMD/IPSL, Université Pierre et Marie Curie, Paris, France, ³KNMI, De Bilt, Netherlands, ⁴LATMOS/IPSL, UVSQ, Versailles, France

Abstract Clouds still remain the largest source of uncertainty in model-based predictions of future climate; thus, the description of the clouds in climate models needs to be evaluated. In particular, the cloud detailed vertical distribution that impacts directly the cloud radiative effect needs to be evaluated. Active satellite sensors directly measure the cloud vertical distribution with high accuracy; their observations should be used for model evaluation together with a satellite simulator in order to allow fair comparison between models and observations. The next cloud lidar in space, EarthCARE/ATmospheric LIDar (ATLID), is planned for launch in 2018, while the current spaceborne cloud lidar CALIPSO/CALIOP is expected to stop collecting data within the next coming years. Here we describe the characteristics of the ATLID on board the EarthCARE satellite (spatial resolution, signal-to-noise ratio, wavelength, field of view, pulse repetition frequency, orbit, and high-spectral resolution lidar) that need to be taken into account to build a Cloud Feedback Model Intercomparison Project Observation Simulator Package (COSP)/ATLID simulator. We then present the COSP/ATLID simulator, and the low-, middle-, high-level cloud covers it produces, as well as the zonal mean cloud fraction profiles and the height-intensity histograms that are simulated by COSP/ATLID when overflying an atmosphere predicted by LMDZ5 global circulation model. Finally, we compare the clouds simulated by COSP/ATLID with those simulated by COSP/CALIPSO when overflying the same atmosphere. As the main differences between ATLID and CALIOP are taken into account in the simulators, the differences between COSP/ATLID and COSP/CALIPSO cloud covers are less than 1% in nighttime conditions

1. Introduction

Clouds are the primary modulators of the Earth's radiation budget and still constitute the main source of uncertainty in model estimates of climate sensitivity [e.g., *Randall et al.*, 2007]. The evolution of cloud properties and the behavior of cloud-related processes in a warming climate remain uncertain [*Intergovernmental Panel on Climate Change*, 2013]. Evaluating against observations the cloud description in climate models is a key first step to test the physical description of clouds in climate models in order to improve models and our trust in model predictions of future climate. As satellites collect observations at global scale, they are a unique tool to evaluate the clouds simulated by climate models. But, the definition of a cloud is different between climate models and satellite observations, it even differs between different satellite instruments [e.g., *Stubenrauch et al.*, 2013] and between different climate models. To bypass these differences in cloud definition and to allow consistent comparisons between clouds simulated by climate models and observed by satellite, the Cloud Feedback Model Intercomparison Project (CFMIP) has developed the CFMIP Observation Simulator Package (COSP) [*Bodas-Salcedo et al.*, 2011], which is composed of satellite simulators that mimic the clouds that would have been observed by different satellites if they were overflying an atmosphere predicted by a climate model. COSP has been widely used for evaluating cloud descriptions in climate models within the CFMIP phase 2/ Climate Model Intercomparison Project version 5 (CFMIP-2/CMIP5) experiment (e.g., <http://cfmip.metoffice.com/>). In particular, COSP contains two active remote sensor simulators: one for CALIPSO [*Chepfer et al.*, 2008] and one for CloudSat [*Marchand et al.*, 2009] that mimic the unique detailed information on the cloud vertical distribution, at a resolution of 480 m, collected by these two missions. The detailed vertical distribution is a key observational constrain for climate models, because it impacts the cloud radiative effect [e.g., *Kato et al.*, 2011; *L'Ecuyer et al.*, 2008; *Chepfer et al.*, 2014], and because it results on first order of the atmospheric circulation at large and small scales.

After Lidar In-Space Technology Experiment collected the first lidar in space observations [*Winker et al.*, 1996] and Ice, Cloud, and land Elevation satellite/Geoscience Laser Altimeter System [*Spinhirne et al.*, 2005], the Cloud Aerosol Lidar and Infrared Pathfinder Satellite Observations (CALIPSO) [*Winker et al.*, 2007] and

CloudSat [Stephens *et al.*, 2002] missions were the first spaceborne lidar and radar missions devoted to cloud studies. Since their launch in 2006, they have collected more than 9 years of observations. CALIPSO is expected to operate for several more years. Earth Clouds, Aerosols and Radiation Explorer (EarthCARE) [Illingworth *et al.*, 2014] is the next mission carrying a lidar (ATmospheric LIDar: ATLID) and a radar (Cloud Profiling Radar) devoted to cloud studies. It is planned to launch in 2018 to operate for a nominal period of 3 to 4 years, and doing so it will extend the spaceborne global-scale lidar record started by CALIPSO in 2006. The CALIPSO + ATLID record will constitute a unique observational data set to study the interannual variability of the detailed cloud vertical distribution associated to large-scale natural climate variability (e.g., El Niño, North Atlantic Oscillation, Madden-Julian Oscillation, and Southern Annular Mode). Moreover, ATLID is a high-spectral resolution lidar (HSRL), which simultaneously and separately measures the thermally-broadened backscatter from atmospheric molecules and the largely unbroadened Rayleigh backscatter from clouds and aerosols [Durand *et al.*, 2007]. This will let ATLID supply accurate extinction and backscatter profiles without assuming the extinction-to-backscatter ratio (as CALIPSO requires), which is poorly known especially for aerosols. In this cloud work, for building the COSP/ATLID simulator we only consider the total backscatter (i.e., the sum of the Rayleigh and aerosol/cloud components) measured by ATLID and not the two channels separately. We will use the separation between the two channels in ATLID actual observations (to be collected from 2018) in order to remove aerosols from ATLID actual observed profiles: this should help avoiding misclassification of heavy aerosol loads as optically thin clouds.

The purpose of this paper is to describe the EarthCARE/ATLID simulator to be included in COSP, to facilitate the evaluation of cloud descriptions in climate models against the spaceborne lidar observations that ATLID will collect during the period 2018–2022.

Even if CALIOP/CALIPSO and ATLID/EarthCARE are both spaceborne lidars, these two missions are different. The main differences are the wavelengths (355 nm for ATLID, 532/1064 nm for CALIOP), the fields of view of the telescopes, the divergences of the laser beam, the optical components (filters, detectors, etc.), the day-night differences, the vertical and horizontal resolution of the lidar profiles, and the high-spectral capability of EarthCARE, and the orbits of the two missions. These differences impact the lidar profiles collected by the two missions, and these differences need to be taken into account in the lidar simulators. In section 2, we first examine the ATLID instrument characteristics, we compute the attenuated backscatter (ATB) and scattering ratio (SR) profiles that ATLID would measure, and we estimate the statistical sampling of profiles collected by ATLID based on its orbit. From this theoretical analysis, we define a first estimate of the cloud detection threshold to apply to ATLID lidar profiles at a given horizontal (232 m) and vertical resolution (480 m), and the number of profiles to be accumulated in a latitude-longitude grid box.

In section 3, we use synthetic mesoscale modeled realistic cloud scenes together with the instrumental EarthCARE Simulator (ECSIM), which mimics ATLID Level 1 data including noise [Donovan *et al.*, 2008], to test the robustness of the cloud detection thresholds determined previously. In particular, we examine the impact of instrumental noise on the cloud detection thresholds for both nighttime and daytime observations.

We then define the COSP/ATLID simulator (section 4) based on the results obtained in sections 2 and 3, and on the heritage from COSP/CALIOP (CALIPSO). Next (section 5), we compare the vertical distribution of clouds seen by COSP/ATLID and by COSP/CALIOP when overflying the same atmosphere predicted by LMDZ5 global circulation model (GCM) [Hourdin *et al.*, 2013].

2. Theoretical Differences Between CALIOP and ATLID Measurements

Here we explore the instrumental and orbital differences between CALIPSO/CALIOP and EarthCARE/ATLID that must be taken into account in the COSP lidar simulator, as they impact the collected total backscatter lidar profiles: the same cloud observed by the two missions will lead to different lidar profiles.

2.1. Wavelength Differences

ATLID's wavelength is 355 nm, and CALIOP's closest laser wavelength is 532 nm. Atmosphere gases do not appreciably absorb radiation at these wavelengths, except ozone at 532 nm. Atmospheric molecular scattering, however, changes strongly with the wavelength.

The scattering efficiency by molecules (Rayleigh regime) is much larger at 355 nm than 532 nm. The Rayleigh backscattering and extinction scale approximately with the inverse fourth power of the wavelength. This

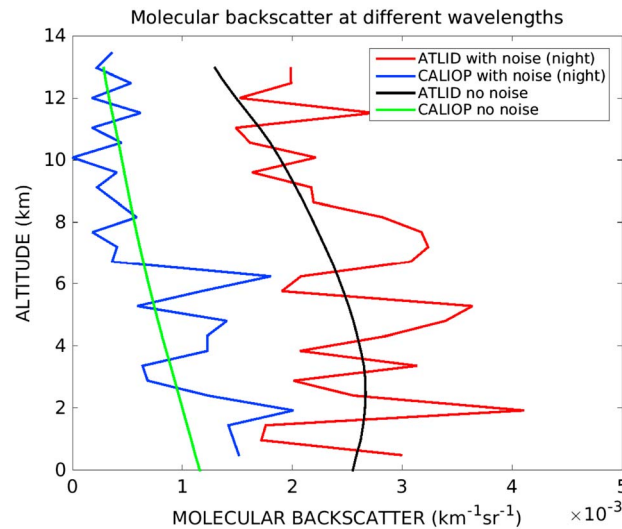


Figure 1. The molecular attenuated backscattered (ATB_{mol}) profiles at 532 nm and 355 nm, without instrumental noise (from the lidar equation) in green and black and with nighttime noise using ECSIM (single-shot profile) in blue and red. The vertical resolution is 480 m (extracted from Figure 4 at $x = 100$ km).

means that molecular backscatter increases by about a factor of 5 going from 532 nm to 355 nm. The lidar signal, however, is also subject to about 5 times more two-way molecular attenuation at 355 nm than at 532 nm [Bucholtz, 1995]. Putting these two factors together, the molecular attenuated backscatter (ATB_{mol}) from a cloud-free and aerosol-free region below 3 km will be about 2 times larger at 355 nm than 532 nm. The lidar equation, including the contribution of molecules and the dependency of the molecular scattering efficiency with the wavelength that have been used to estimate this number, is given in Appendix A. Examples of the ATB_{mol} at 532 nm and 355 nm, computed directly from the ECSIM pressure and temperature profiles using the lidar equation (Appendix A), are plotted in Figure 1. The ATB_{mol} at 532 nm (green line) increases somewhat linearly, while the ATB_{mol} at

355 nm (black line) is curved. The increase from 13 km to 3 km is due to the more important contribution of molecules at 355 nm as the signal reaches lower atmospheric layers. Note that the curve inversion and signal decrease below 3 km at 355 nm, due to attenuation.

To detect particles, we use the scattering ratio $SR(\lambda, z)$, defined as the ratio between the total attenuated backscatter $ATB(\lambda, z)$ (including molecules and particles), over the molecular-only attenuated backscatter $ATB_{mol}(\lambda, z)$ (Appendix A). This ratio is equal to 1 in the absence of aerosol and cloud ("pristine" conditions) at altitudes above cloud/aerosol attenuation ($\beta_{part}(\lambda, z) = \alpha_{part}(\lambda, z) = 0$) and is greater than 1 in presence of particles and/or aerosols. This ratio can be below 1 in clear-sky areas if the lidar signal has been attenuated by higher-altitude cloud or aerosol layers.

Because (i) the contribution of molecules to the ATB is larger at 355 nm than 532 nm, and (ii) the contribution of cloud particles to the ATB is similar at 355 nm and 532 nm, the relative contribution of particles compared to molecules is larger at 532 nm than 355 nm (by a factor of ~ 5). As a consequence, for a same idealized cloud, SR_{355} (ATLID) will be smaller than SR_{532} (CALIOP). Thus, to detect a given cloud, a smaller SR threshold should be used for ATLID data. In practice, the lower bound of the ATLID detection threshold will depend on the noise characteristics of ATLID. The shift in wavelengths also has a consequence for the signal-to-noise ratio (SNR) of the scattering ratios. Generally, even if the SNR associated with the attenuated backscatter measurements are similar at 532 and 355 nm, for scattering ratios in the green (532 nm) less than about 5, the SNR associated with the 532 nm measurement can be substantially higher than the corresponding 355 nm value. This is discussed in more detail in Appendix A.

2.2. Multiple Scattering Differences

The magnitude of multiple scattering effects depends on the lidar altitude, the telescope field of view (θ_{FOV}), and laser beam divergence. It also depends on the properties of the probed cloud: its morphology (vertical and horizontal extension) and the types of particles within the cloud (size, shape, density, and orientation in space) [e.g., Eloranta, 1972; Noel et al., 2002; Hogan, 2006]. Since, for instance, the altitude of CALIOP is 705 km and its θ_{FOV} 130 μ rad [Hunt et al., 2009], versus an altitude of 393 km and a θ_{FOV} of 75 μ rad for ATLID [Hélière et al., 2012], the ATB observed by ATLID and CALIOP from a cloud of same properties will be differently affected by multiple scattering.

The multiple scattering coefficient (η [Platt, 1973]) is often used in the literature to simply account for multiple scattering effects: $\eta = 1$ corresponds to single scattering only, and η decreases as multiple scattering effects increase (see Appendix A). Hereafter, we estimate the differences between ATLID and CALIOP multiple

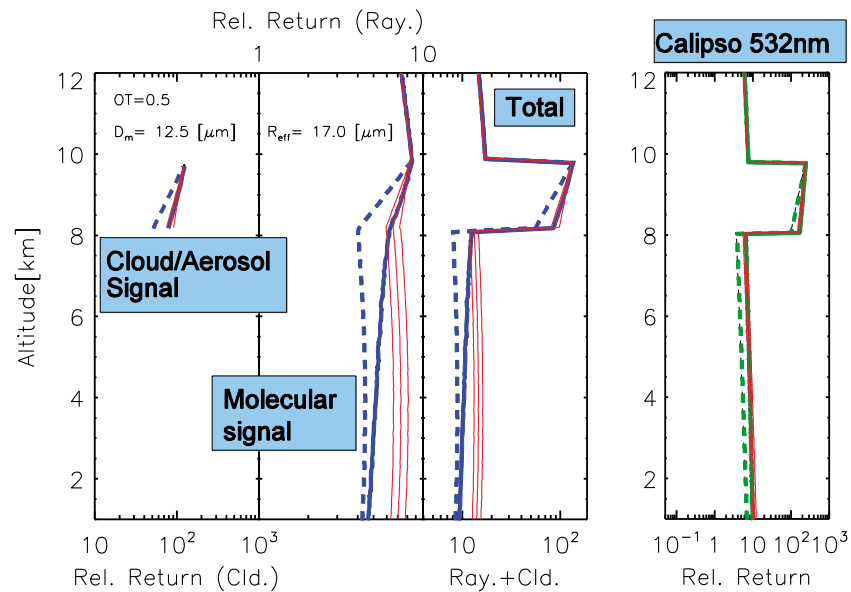


Figure 2. Results of Monte Carlo lidar radiative transfer simulations for ATLID (blue lines) and for CALIPSO (green lines) compared to the single-scatter signal (dotted lines) and compared to equation (A1) with $\eta = 0.4, 0.5$, and 0.6 (red-lines). For ATLID the results for the particle (cloud/aerosol) profile and the molecule (thermally broadened Rayleigh channel) profile are shown along with the total (particles + molecules) profile.

scattering effects *within* the cloud, because they impact the ATB and SR profiles (see equations in Appendix A) used to detect clouds (see next section). We estimate η_{atlid} and η_{caliop} for the same cloud, using Monte Carlo simulations including high scattering orders.

2.2.1. Monte Carlo Model

Since the lidar footprint is large compared to the photon mean-free-path and photons tend to stay within the receiver cone due to the strongly forward-scattering nature of cloud particle phase functions, several orders of scattering can significantly contribute to the lidar signal [Hogan, 2006].

In order to further investigate the effects of multiple scattering (MS) on ATLID versus CALIOP signals, we used the ECSIM lidar Monte Carlo (MC) forward model. ECSIM is a modular multisensor simulation framework, originally developed in support of EarthCARE but flexible enough to be applied to other instruments and platforms [Voors *et al.*, 2007]. The MC model is similar to the one described by Hu *et al.* [2001] and can in addition predict the spectral-polarization state of the lidar signal. The ECSIM MC code has been compared to other codes as well as CALIPSO observations with generally excellent agreement being found [Petzold *et al.*, 2011]. The ECSIM lidar MS radiative transfer model and lidar instrument model are described in more detail in Appendix B.

2.2.2. Multiple Scattering Differences Between ATLID and CALIOP

Example results of MC calculations applied to an idealized cirrus cloud are shown in Figure 2. We used an idealized cloud of optical thickness of 0.5, made of hexagonal ice crystals [Hess *et al.*, 1998b] with a gamma size distribution and associated mean diameter (diameter being the crystal maximum length) of $12.5 \mu\text{m}$. The corresponding effective radius (R_{eff}) values are shown in the plot with R_{eff} for the nonspherical ice crystals defined according to Francis *et al.*, 1994. MC lidar radiative transfer results (to 10 orders of scattering) are shown as well as results corresponding to single scattering only and the result of applying equation (A1) with three different values of the multiple-scattering coefficient. Results for the separate HSRL channels for ATLID as well as the resulting total signal (including the depolarized signal) are shown as the corresponding 532 nm CALIPSO signals.

Figure 2 shows that equation (A1) with values of the MS coefficient between 0.4 and 0.6 perform well within the cloud for both CALIPSO and ATLID. However, in the case of ATLID, the limitations of equation (A1) become apparent: the Rayleigh signal below cloud base displays a “decay” toward the single-scatter signal level. The decay is the result of the cloud, acting as a second source of photons which emerge from cloud

base with a certain effective angular divergence. The decay in this example is not very noticeable in the CALIPSO simulation (the multiple scattered light emerging from the cloud tends to stay within the lidar field of view for CALIPSO but less so for the narrower ATLID field of view). For CALIPSO the decay becomes more noticeable as the optical thickness of the cirrus cloud increases and, as discussed in Appendix B, even becomes obvious in the CALIPSO simulations for small particle sizes and larger optical depth.

MC simulations carried out using idealized water clouds (see Appendix B) show that like with cirrus clouds, equation (A1) with an appropriate value of MS coefficient performs well *within* clouds. However, mainly due to the smaller particle sizes associated with water drops compared to cirrus clouds, both the ATLID and CALIPSO simulations exhibit obvious decays below cloud base, which cannot be modeled using equation (A1). This finding, however, is of little practical significance to this work as the majority of warm water clouds are often opaque to both CALIPSO and ATLID so their base is rarely observed.

Despite the limitations described above of the approach embodied by equation (A1) to model the backscatter below high clouds, the MS coefficient approach is still considered useful for the purposes of this work. It is easy to implement and computationally fast. For the CALIPSO configuration, it is reasonably accurate even below the cloud in the presence of thick cirrus. For ATLID, some inaccuracies may be encountered in the presence of low-altitude clouds below thick cirrus. Still, the end results may not be strongly affected as low-level water clouds are bright targets: their attenuated backscatter is expected to rise above any reasonable detection threshold despite inaccuracies in the MS treatment. Exceptions may occur, such as with low-level water clouds with low optical depths, but those are rare.

2.2.3. Spatial Resolution Differences

Cloud and aerosol detection methods are usually based on thresholds [e.g., Vaughan *et al.*, 2009; Winker *et al.*, 2010; Hagihara *et al.*, 2010] that are highly sensitive to the vertical [Chepfer *et al.*, 2010] and horizontal resolutions of the profiles [e.g., Chepfer *et al.*, 2013, Figure 1] and the SNR. The planned nominal resolutions of ATLID profiles are 282 m horizontally and 100 m vertically. The nominal resolution of CALIOP ATB profiles is 330 m horizontally and 30 m vertically below 8.2 km of altitude, and 60 m vertically and 1 km horizontally above 8.2 km of altitude. At nominal resolution, the SNR is usually too low for detecting clouds, so the profiles are first averaged at coarser resolution, either horizontally or vertically [Chepfer *et al.*, 2013] before detecting clouds. For the purpose of climate model evaluation, it is desirable to keep the full horizontal resolution [Chepfer *et al.*, 2008] and to increase the SNR by averaging the lidar profile vertically. The COSP/CALIPSO simulator uses SR profiles regridded on the vertical in 480 m bins to have consistent resolution with the CFMIP-2 multimodel experiment [Bony *et al.*, 2009]. This vertical resolution is also the least common multiple of CloudSat (480 m) and CALIPSO-GOCCP (16 vertical levels of 30 m). Consistently, with these previous works, we will consider for the current study the ATLID profile vertically regridded over 480 m or 500 m (the closest multiple of 100 m, nominal resolution of ATLID).

2.2.4. Profile Sampling Differences Between ATLID and CALIOP, Consequences for Gridded Products

The distance between two successive ATLID profiles is 282 m versus 333 m for CALIOP. Two instrumental characteristics explain this difference. First, the pulse repetition frequency (PRF) of ATLID is 51 Hz. ATLID backscatter profiles are averaged two by two, leading to an equivalent PRF of ~25 Hz. The lower PRF for CALIOP (20 Hz) means that ATLID profiles should be closer to each other. However, the orbital differences between the two spacecraft (ATLID is ~300 km lower than CALIOP) mean that the EarthCARE platform travels ~7% faster, which increases the distance between profiles and somewhat balances the previous effect. Due to these differences, both instruments will measure a different number of profiles in a fixed geographical area over the same period of time. Figure 3 documents the geographic differences in the number of profiles measured by each instrument over an arbitrary period.

Figure 3 shows that over the same period of time, ATLID will measure ~25% more profiles than CALIOP on average in the $\pm 60^\circ$ latitude band. Over 3 months, this translates to ~130,000 more profiles. The geographic density of profiles measured by ATLID will be lower in the polar regions close to $\sim 80^\circ$, but EarthCARE will reach slightly higher latitudes (83° versus 82° for CALIOP).

A cloud flagged profile from ATLID is equivalent to a cloud flagged profile from CALIOP. Since ATLID obtains more profiles than CALIOP in a similar time period, acceptable levels of statistical representativity for a given geographic area will be reached faster with ATLID than with CALIOP. For instance, aggregating 3 months of cloud flag profiles from GOCCP is necessary to derive representative cloud distribution statistics in $2^\circ \times 2^\circ$ at a global scale. The same level of representativity will be reached by aggregating ATLID data over merely

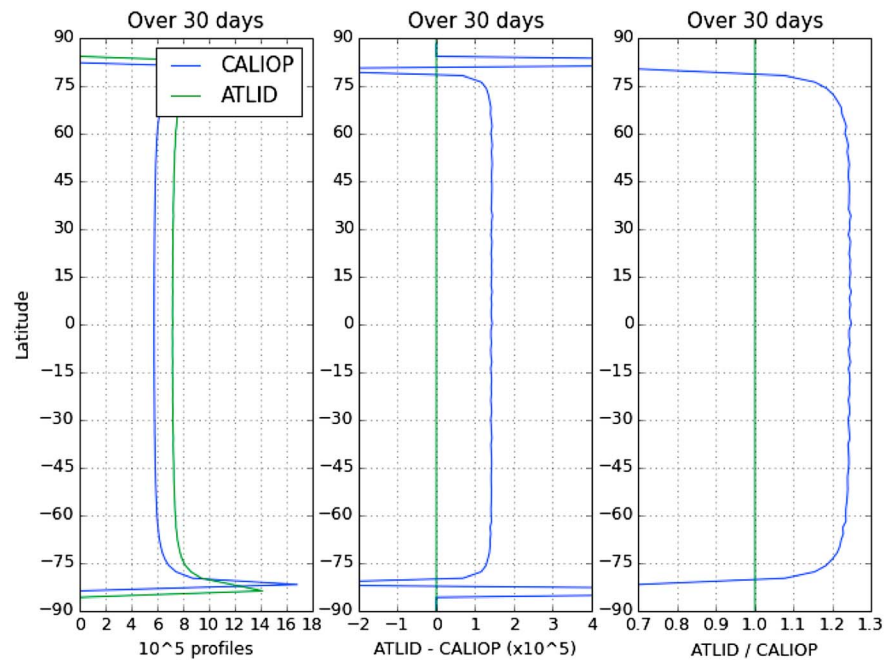


Figure 3. Number of profiles measured by (left) both instruments, (middle) difference between both, and (right) ATLID versus CALIOP fraction in 2° latitude bins. Orbital trajectories were calculated over 3 months for both spacecraft by the Ixion software (<http://climserv.ipsl.polytechnique.fr/ixion.html>) considering their known and planned properties at the time of writing. We used a PRF of 25 Hz for ATLID and 20 Hz for CALIOP.

67 days. Conversely, over similar observation periods ATLID products will be statistically representative in smaller geographic regions than CALIOP: over 3 months, ATLID global cloud distribution at $\sim 1.75^\circ \times 1.75^\circ$ will be as representative as CALIPSO's at $2^\circ \times 2^\circ$.

3. Estimate of the Cloud Detection Threshold to be Used in COSP/ATLID

The cloud detection threshold is applied to a single SR profile; it depends on the vertical resolution of the profile and on the signal-to-noise ratio. The same thresholds are applied consistently between observations and simulations (with COSP). In this section we estimate the best guess before launch for this threshold number. It differs between nighttime and daytime data, as these later are contaminated by solar photons.

3.1. Methodology: Case Studies Over Synthetic Mesoscale Cloud Scenes

We use synthetic model cloud scenes producing a highly detailed structure of the cloud field. The ECSIM simulator [Donovan *et al.*, 2008], developed to study instrument design and performance, is used to mimic the ATLID instruments. COSP/lidar [Chepfer *et al.*, 2007, 2008; Chiriaco *et al.*, 2006] differs from ECSIM [Donovan *et al.*, 2008] in the following aspects: COSP/lidar does not include instrumental noise, has a fixed vertical resolution, uses a simple processing of multiple scattering based on a η value, contains a cloud detection in each profile, contains global cloud statistical diagnostics (maps, etc.), is embedded in COSP with other satellite simulators, and has been designed and optimized for long-term climate simulations. We used ECSIM to produce lidar profiles that include instrumental noise, at the nominal resolution of ATLID for each cloud scene. Using these synthetic lidar profiles, we test the possibility (and limits) of detecting clouds with ATLID in relevant cloud scenes (cirrus and shallow cumulus), taking into account the SNR of the instrument. For cloud detection, we first compute the ATB and ATB_{mol} profiles at the original resolution of the instrument, we then follow the COSP/ATLID steps: (i) compute the ATB and ATB_{mol} profiles at 480 m vertical resolution, (ii) compute the SR profile at 480 m vertical resolution, and (iii) detect the cloud using threshold values of SR.

3.1.1. About the Molecular Profiles

We singled out cloud-free and aerosol-free ATB_{mol} profiles (Figure 1) within the complete atmospheric scene (second white vertical line in Figure 4a) to quantify the impact of instrumental noise in ATLID molecular

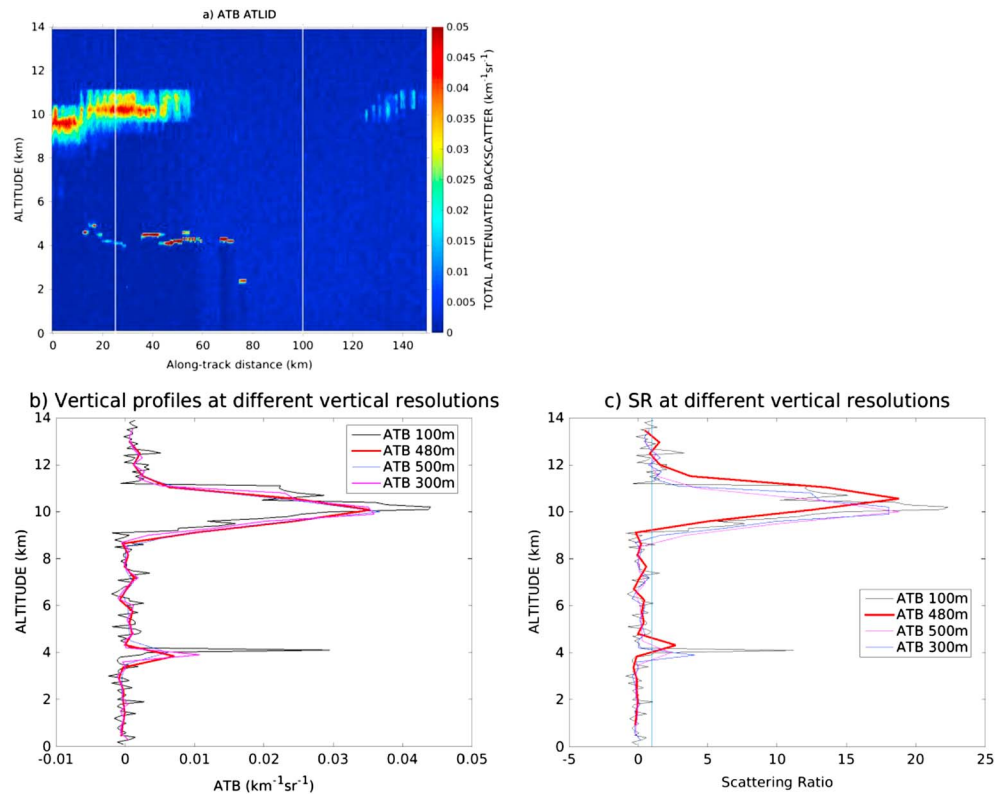


Figure 4. Cirrus cloud case (a and b) total attenuated backscatter (ATB) for ATLID at full resolution. The left white lines indicate the position of the ATB profile shown in Figure 4b at different vertical resolution. (c) The same profile as in Figure 4b but in SR. The simulations here correspond to nighttime conditions.

profiles. The vertical average of no-noise ATB_{mol} profile is $2.2 \cdot 10^{-3} \text{ km}^{-1} \text{ sr}^{-1}$ when the noisy one from ECSIM is $2.4 \cdot 10^{-3} \text{ km}^{-1} \text{ sr}^{-1}$. The noise level, defined as the signal standard deviation along the vertical, is $6.3 \cdot 10^{-4} \text{ km}^{-1} \text{ sr}^{-1}$. In addition yielding an average SNR of about 3.5. Here nighttime conditions have been assumed for the calculation of background noise.

3.2. A Cirrus Cloud Night Case: COSMO

Cirrus clouds are often optically thin, making them difficult to accurately quantify with passive remote sensing and a key target for lidar in space observations.

3.2.1. ATB and SR Profiles

Figure 4a show ATLID nighttime ATB profiles simulated by ECSIM from a scene containing high-altitude clouds between 8 km and 12 km, at the nominal vertical resolution of the instrument (100 m). The scene is originally derived from Deutsche Wetter Dienst COSMO (Consortium for Small-scale Modeling) output [Placidi *et al.*, 2010]. In the cirrus clouds, ATB values reach $0.04 \text{ km}^{-1} \text{ sr}^{-1}$ (Figure 4b).

ATB profiles are averaged vertically from 100 m to 480 m (Figure 4b), which increases the SNR while smearing cloud boundaries, and can prevent detection for weakly scattering layers. From these ATB and ATB_{mol} , we compute the corresponding SR profiles (Figure 4c). The maximal intensity for ATLID is about $SR = 22$ for cirrus cloud around 10 km of altitude and is reduced to $SR = 18$ when vertically averaged. The maximal SR peak values is between 20 and 23 in the cirrus layer and between 3 and 10 in the boundary layer cloud, depending on the vertical resolution used (100 m to 500 m). It shows that using 500 m (a multiple of ATLID vertical resolution) or 480 m (a multiple of CALIOP resolution) leads to very similar ATB and SR profiles. As a consequence, in the rest of the paper we will present results at 480 m.

3.2.2. Cloud Detection

We define the cloud detection threshold as 3 times the standard deviations of the nighttime values of SR above the clear-sky baseline ($SR = 1$). The SR standard deviation is computed from 10 clear-sky profiles,

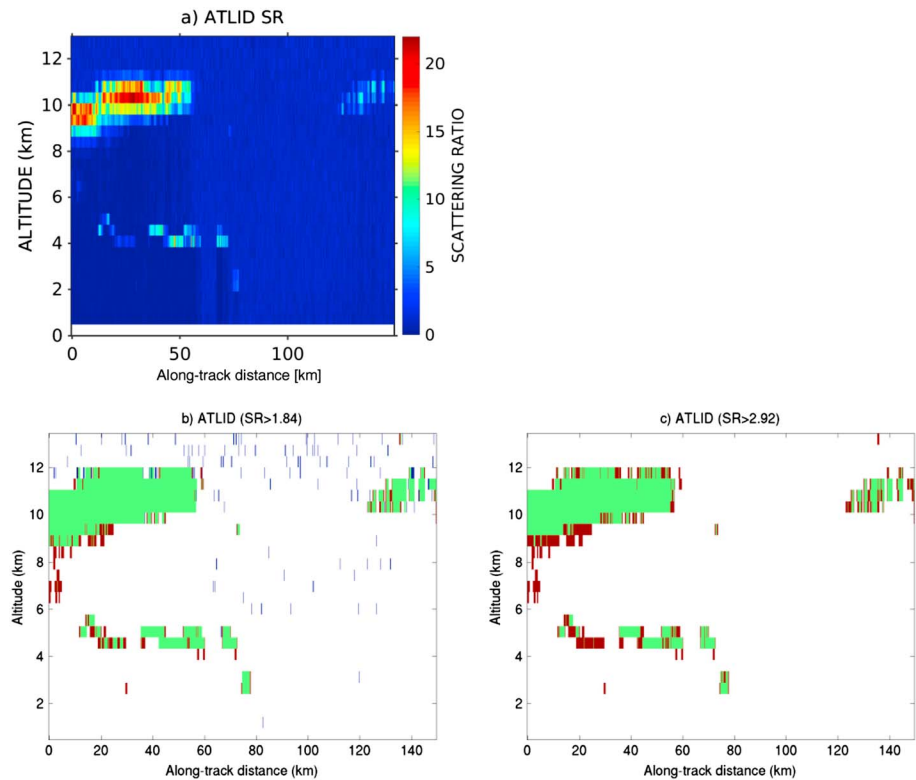


Figure 5. Cirrus case as in Figure 4. Sensitivity of the cloud detection to the value of the cloud detection threshold. (a) SR values. (b and c) SR mask during nighttime condition with $SR_{\text{Night}} > 1.84$ and during daytime condition with $SR_{\text{Day}} > 2.92$, respectively. False negatives are in red, while false positives are in blue. Cloud mask indicated in green.

between 100 km and 104 km along track in the COSMO scene (Figure 5b). It results that an atmospheric layer is declared cloudy when $SR_{\text{NIGHT}} > 1.84$. Applying this cloud detection to the COSMO case in nighttime (Figure 5b) leads to some false detections occurring at higher altitudes. These false-positives at low scattering ratio (which are at a higher occurrence rate than for CALIPSO) are a consequence of the much higher amounts of Rayleigh scattering at the ATLID wavelength of 355 nm and its impact on the SNR of the scattering ratios, as discussed in Appendix A.

For daytime data, we define another threshold, hereafter called “daytime threshold,” as 3 standard deviations of the SR daytime profiles for ATLID above the clear-sky baseline: $SR_{\text{DAY}} > 2.92$. This threshold leads to almost no false detections (Figure 5c). Hereafter, we consider this ATLID daytime threshold ($SR_{\text{DAY}} = 2.92$) as the main constraint to limit false detections.

3.3. A Shallow Cumulus Night Case: ASTEX

Low-level sparse shallow cumulus are another key target for lidar in space observations [e.g., Konsta *et al.*, 2012]. In 1992, the ASTEX campaign (Atlantic Stratocumulus Transition Experiment) sought to improve the understanding of physical and radiative properties of boundary layer clouds and marine stratocumulus. Simulations based on this campaign were generated and used as ECSIM inputs. The simulation, based on profile samples along a satellite track through the cloud field simulated by a large eddy simulation model containing shallow cumulus in nighttime, is presented in Figure 6a. No high clouds are present in this simulation.

We investigate the efficiency of the cloud detection SR thresholds defined previously (section 3.2). In nighttime conditions, the cloud detection threshold ($SR_{\text{NIGHT}} > 1.84$) leads to some false detections just above shallow cumulus clouds and above 10 km (Figure 6b). In daytime conditions, considering more noise (not shown) than in nighttime, the cloud detection threshold ($SR_{\text{DAY}} > 2.92$) leads to very few false cloud detections (Figure 6c).

Additional detailed information on the sensitivities of the false positive and false negative cloud detections, to the value of the cloud detection threshold, are given in Figure C4 for ASTEX and COSMO cases.

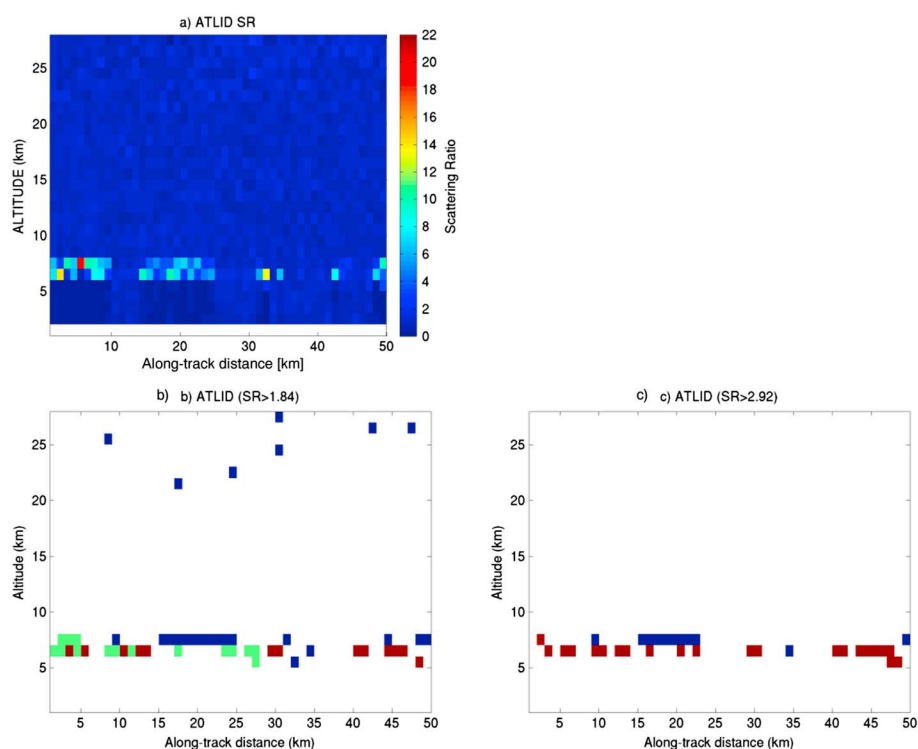


Figure 6. Same as Figure 5 but for a shallow cumulus case.

4. Differences Between COSP/ATLID Simulator and COSP/CALIPSO Simulator

4.1. About COSP/CALIPSO

The COSP/CALIPSO software simulates the ATB and ATB_{mol} (at 532 nm) over 40 vertical levels (480 m vertical resolution) in $2^\circ \times 2^\circ$ horizontal grid boxes from subgridded GCM outputs. Clouds are detected in each profile using $SR > 5$ (consistently with CALIPSO-GOCCP). Cloudy pixels are accumulated over $2^\circ \times 2^\circ$ latitude-longitude

Table 1. Set of Cloud Detection Thresholds Used for Global Scale Analysis (Section 5) and Corresponding High and Low Cloud Covers^a

| | ATLID | CALIPSO |
|--------------------------------|--|--|
| Reference detection thresholds | SR > 1.84 | SR > 5.51 |
| Justification from | ATLID nighttime noise standard deviation at 355 nm | Equivalent for CALIPSO at 532 nm |
| High cloud cover | Mean: 28.1% | Mean: 28.2% |
| | | Maximum local difference: 1.7% |
| | | Cloud cover relative differences: 0% |
| Low cloud cover | Mean: 15.3% | Mean: 15.8% |
| | | Maximum difference: 2.4% |
| | | Cloud cover relative differences: 0% |
| Daytime detection thresholds | SR > 2.92 | SR > 11.34 |
| Justification from | ATLID daytime noise standard deviation at 355 nm | Equivalent for CALIPSO at 532 nm |
| High cloud cover | Mean: 27.3% | Mean: 27.3% |
| | | Maximum difference: 3.8% |
| | | Cloud cover relative differences: 0% |
| Low cloud cover | Mean: 13.6% | Mean: 13.6% |
| | | Maximum difference: 2.8% |
| | | Cloud cover relative differences: 0.6% |

^a"Cloud cover relative differences" refer to the differences between GCM + COSP/CALIPSO and GCM + COSP/ATLID (GCM + COSP/CALIPSO as reference) cloud covers.

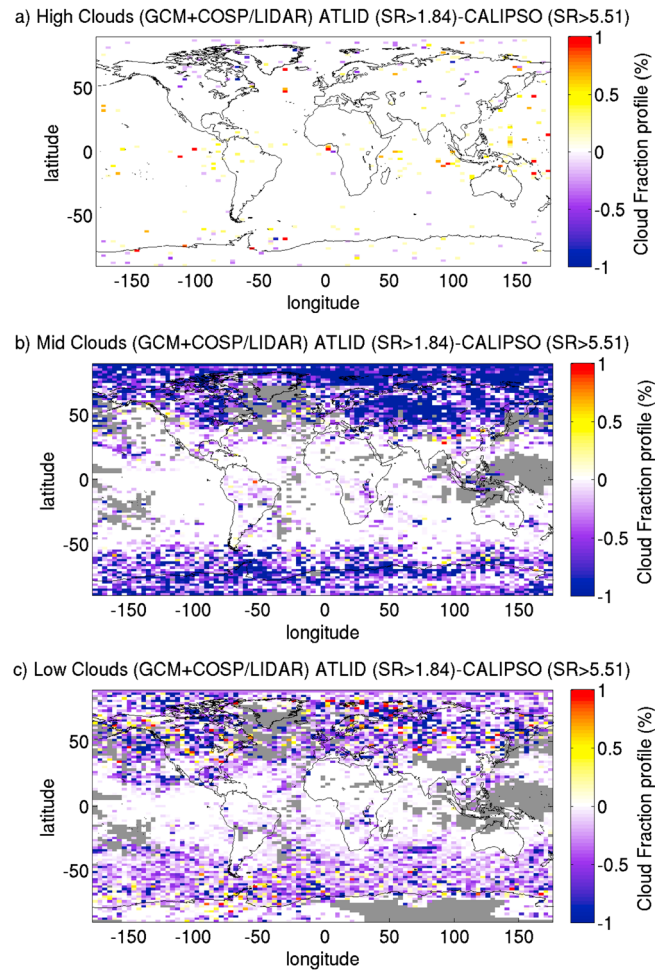


Figure 7. Differences between cloud covers from GCM + COSP/ATLID and GCM + COSP/CALIPSO in January. (a) High-level, (b) middle-level, and (c) low-level cloud. COSP/ATLID uses $\eta = 0.6$ and $SR_{NIGHT} = 1.84$. COSP/CALIPSO uses $\eta = 0.7$ and $SR = 5.51$. Missing data are in grey.

gridboxes to build the cloud covers (low, middle, high, and total) and the cloudy profiles. Version 1.3 of COSP/CALIPSO is intensively used within the CFMIP-2 [Bony *et al.*, 2009] and CMIP-5 experiments. It uses a multiple scattering factor of $\eta = 0.7$. The sensitivities of the cloud cover to these two parameters have small impact on cloud fraction [e.g., *Chepfer et al.*, 2008, 2010, 2013; *Cesana and Chepfer*, 2013]: A difference of less than 1% is observed when changing the η factor from 0.3 to 0.7. The change in η (0.7 to 0.3) affects the vertical cloud profile just below the maximum of cloud fraction by 11% maximum. No drastic change in cloud fraction is observed when switching the cloud detection threshold from $SR = 5$ to $SR = 3$ in LMDZ5, which suggests that this model does not simulate many optically thin clouds.

4.2. About COSP/ATLID

We adapted the CALIPSO in space simulator [Chepfer *et al.*, 2008] included in COSP [Bodas-Salcedo *et al.*, 2011] to mimic the total and low-, middle-, and high-level cloud covers and the cloud fraction profile that ATLID would observe if it was overflying the atmosphere predicted by the LMDZ5B GCM [Hourdin *et al.*, 2013] in January. The GCM outputs come from an Atmospheric Model Intercomparison Project-like simulation, without ocean-atmosphere coupling, and SST forced by observations.

COSP/ATLID simulator is at 355 nm instead of 532 nm COSP/CALIPSO: this means that ATB_{mol} and ATB profiles are computed at 355 nm in COSP/ATLID as discussed in section 2.1. The multiple scattering factor was changed from $\eta = 0.7$ to $\eta = 0.6$ in accordance with MS computation (section 2.2). For the SR cloud detection threshold, we consider two situations (Table 1): (i) the nighttime ($SR_{NIGHT} > 1.84$) and (ii) the daytime ($SR_{DAY} > 2.92$). The daytime threshold could be used for comparison between GCM + COSP/ATLID outputs with ATLID observations collected in both daytime and nighttime, whereas the nighttime threshold can be applied for comparison with nighttime ATLID observations only (less noise).

The low-, mid-, and high-level cloud maps obtained from LMDZ + COSP/ATLID as well as the cloud fraction profiles and the height-intensity histograms are presented in Appendix C (Figures C1, C2, and C3). Figure C3 shows that there is no low-level liquid clouds with $SR > 17.2$ for ATLID (this corresponds to $SR > 80$ for CALIPSO) because of the attenuation of the lidar signal within the cloud. Contrarily to the radar, the lidar signal is attenuated (see equation (A1) right end side): the backscatter term (β) competes with the attenuation term (exponent). Hence, when α increases, the ATB (and SR) reaches a limit where the attenuation term will dominate the backscatter term. The exponential will tend to 0 and so will do the SR (and ATB) too. Moreover, we also studied the sensitivity of the cloud cover (Figure C1) to the value of the multiple-scattering factor (not shown): it results that using $\eta = 0.7$ or $\eta = 0.6$ in the COSP/ATLID changes the cloud covers (Figure C1) by less than 0.5%.

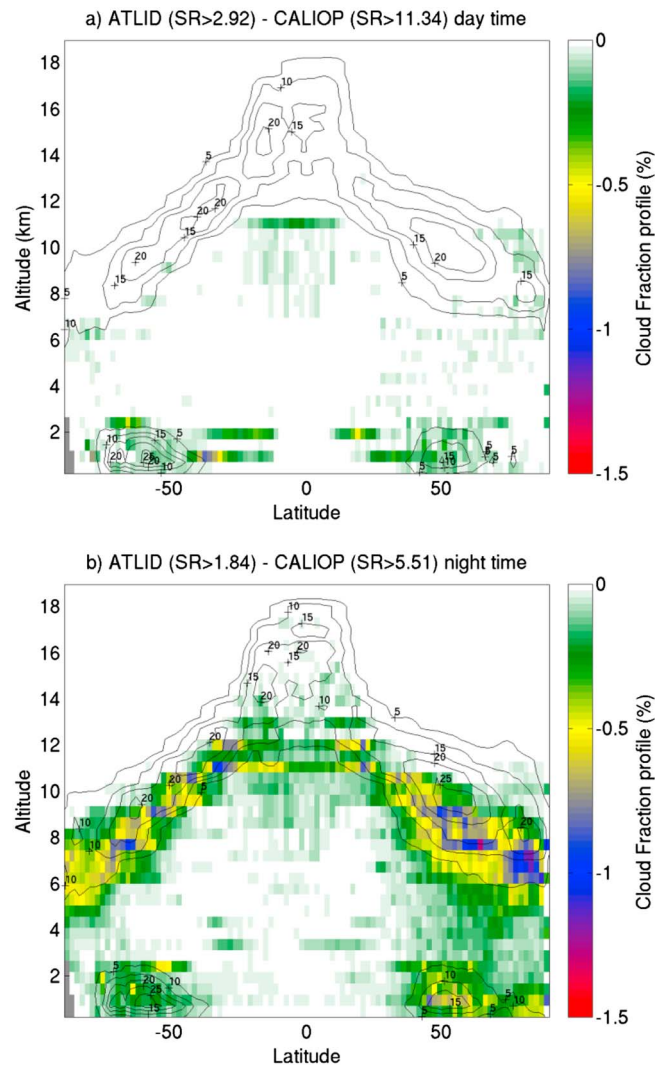


Figure 8. Differences between the zonal cloud fraction profiles from GCM + COSP/ATLID and GCM + COSP/CALIPSO in January. (a) In daytime COSP/ATLID uses $\eta = 0.6$ and $SR_{DAY} = 2.92$, whereas COSP/CALIPSO uses $\eta = 0.7$ and $SR = 11.34$. (b) In nighttime COSP/ATLID uses $\eta = 0.6$ and $SR_{NIGHT} = 1.84$, whereas COSP/CALIPSO uses $\eta = 0.7$ and $SR_{DAY} = 5.51$.

like and CALIPSO-like low cloud covers in nighttime are shown in Figure 7c. ATLID-like finds typically a slightly smaller low cloud cover than CALIPSO-like (-0.3%), especially over midlatitudes and polar regions. In global mean, this difference is -0.2% (Table 1). Difference between ATLID-like and CALIPSO-like midlevel cloud covers (Figure 7b) is typically 1% at latitudes higher than 50° . Table 1 summarizes the absolute and the relative differences between ATLID-like and CALIOP-like maps when considering nighttime cloud detection thresholds and daytime cloud detection thresholds. The maximum absolute differences are less than 3.8% for high cloud covers and 2.8% for low cloud covers in nighttime. The relative differences are 0.6% at most, for the low-level clouds in nighttime.

The differences between the ATLID-like and the CALIPSO-like cloud fraction profiles are shown in Figure 8a for daytime (in colors), with isolines showing the ATLID-like cloud fraction profiles (from Figure C2a). The largest differences do not occur where the cloud fraction is maximal but slightly below, after the laser has penetrated upper cloud layers. ATLID-like zonal cloud fraction profiles is slightly smaller than CALIOP-like zonal cloud fraction profiles ($CF_{ATLID} - CF_{CALIOP} < -0.5\%$) along the Intertropical Convergence Zone (ITCZ) at 11 km of altitude and in the subsidence tropical boundary layer clouds. In nighttime (Figure 8b), the

5. Differences Between Clouds From COSP/ATLID and COSP/CALIPSO Over a Same Atmosphere at Global Scale

For a same atmosphere, ATLID and CALIPSO are not expected to observe the same SR profiles because of instrumental differences between the two lidars. They may hopefully give similar cloud maps and fraction profiles if instrumental differences are (in part) taken into account in the data processing.

This is the approach that is reproduced within simulators: for a given GCM LMDZ atmosphere, the SR_{ATLID} from COSP/ATLID and $SR_{CALIPSO}$ from COSP/CALIPSO will be significantly different because the instruments are different, but it does not preclude COSP/ATLID and COSP/CALIPSO cloud maps (and cloud fraction profiles) to be similar because the instrumental differences are taken into account within the simulators by considering different consistent cloud detection thresholds for COSP/CALIPSO and COSP/ATLID (Table 1).

Here we quantify the residual difference between LMDZ + COSP/ATLID clouds and LMDZ + COSP/CALIPSO clouds when using the detection thresholds listed in Table 1.

In nighttime, the difference between the ATLID-like and the CALIPSO-like high cloud covers (Figure 7a) is 1% at most and scattered throughout the entire surface of the globe. In global mean the absolute difference is 0.4% (Table 1). Differences between ATLID-

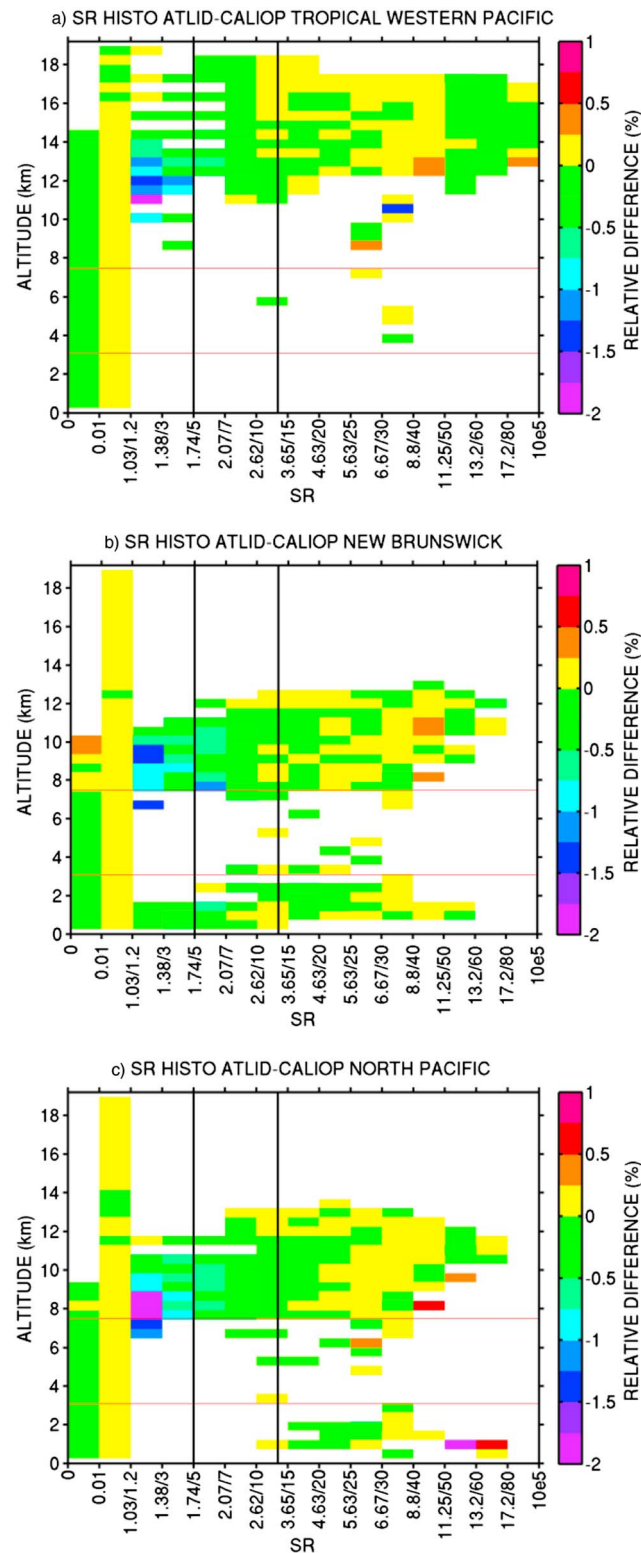


Figure 9. Relative differences of SR histograms between COSP/ATLID and COSP/CALIOP in the same regions as in Figure 9. Note that abscise ticks contain the values of the ATLID SR bins/the values of the corresponding CALIOP SR bins. Black vertical lines shown $SR_{ATLID/NIGHT} = 1.84$ and $SR_{ATLID/DAY} = 2.92$ thresholds. Red lines correspond to the low-middle and middle-high separations.

differences between the ATLID-like and the CALIPSO-like cloud fraction profiles can reach up to 1% below the maximum of cloud fraction profiles. ATLID-like cloud fraction profile detects less clouds than CALIOP-like cloud fraction profile above midlatitude and pole regions ($CF_{ATLID} - CF_{CALIOP} \sim -0.5\%$). The differences between ATLID-like and CALIOP-like cloud profiles is larger during nighttime than during daytime, consistently with Figure 9 showing that the number of occurrences falling between the daytime and nighttime detection thresholds (two vertical lines in Figure 9) is slightly higher for CALIOP-like than for ATLID-like cloud fraction profiles. The relative difference of occurrence ($(ATLID - CALIOP)/ATLID$; Figure 9) is typically 0.5: green boxes located between the two detection thresholds (vertical lines).

6. Conclusions

The mean state and the variability of the cloud detailed vertical distribution is a key variable that must be evaluated in the cloud description of climate models. The ATLID spaceborne lidar on board the EarthCARE satellite is expected to start collecting data in 2018 and will measure directly the cloud detailed vertical distribution. The current study introduces the spaceborne ATLID simulator to be included in COSP to facilitate the use of ATLID data for evaluating cloud descriptions in climate models.

In the first part, we showed how the wavelength difference between ATLID and CALIOP impacts the intensity of the lidar Level 1 ATB_{mol} profiles, ATB profiles, and SR profiles (by a factor of 2 to 5). Then we examined the differences in the multiple scattering between ATLID and CALIOP and showed that a multiple-scattering coefficient of 0.6 can be used in both cases without significant differences within the clouds. We also showed that the differences in the altitudes of the two satellites (more than 300 km) and the frequencies of the laser pulse of the two instruments should lead to a

difference of 20% in the number of lidar profiles accumulated in each latitude-longitude grid box. Finally, we estimated the thresholds to be applied to ATLID SR profiles to detect clouds, taking into account the ATLID SNR (predicted at the time of writing) and vertical resolutions used in current climate model evaluation (480 m vertical), although the vertical resolution could be increased in the future. For this purpose, we used two synthetic mesoscale model cloud scenes, one over a cirrus cloud and one over a shallow cumulus clouds field, together with the ECSIM, which simulates the lidar radiative transfer and instrumental noise to predict what ATLID would observe above cirrus and shallow cumulus at nominal resolution (282 m horizontal and 100 m vertical). Then, we degraded the vertical resolution of these profiles to 480 m to increase the SNR. We obtained two best estimates of cloud detection thresholds to be applied on 480 m SR ATLID profiles: one for nighttime ($SR_{NIGHT} = 1.84$) and one for daytime ($SR_{DAY} = 2.92$). SR_{DAY} is larger than SR_{NIGHT} because solar photons impact the SNR in daytime for a given set of vertical/horizontal resolutions. As it is impossible to definitively decide the proper thresholds at this point since the satellite is not launched yet, we will revisit these cloud detection thresholds after EarthCARE launch based on the actual ATLID signal quality and SNR. In particular, we will use the first year of ATLID Level 1 data to build a statistically significant estimate of the ATLID actual SNR in aerosol-free stratosphere areas, during daytime and during nighttime over different regions, different seasons, and over different surface types (ocean, continent, and ice sheet) as well as above highly reflecting low-level liquid clouds. These information will be used to test and change [as in, e.g., Noel et al., 2014; Chepfer et al., 2010] the threshold values consistently in the simulator and in the algorithm to be used for processing ATLID actual data. In any case, because of the solar photons, the daytime cloud detection threshold will be applicable for comparison with profiles collected in both daytime and nighttime, whereas the nighttime threshold will be applicable for comparison with profiles collected in nighttime data only.

In the second part of this study, we built the COSP/ATLID simulator based on the COSP/CALIPSO simulator. We changed the wavelength, the multiple-scattering parameterization, and the cloud detection thresholds, as discussed here above. Then, we built global-scale cloud properties that would be observed if ATLID was overflying a given atmosphere simulated by the LMDZ5 GCM: maps of low-, middle-, and high-level clouds; zonal cloud fraction profiles; and height-SR histograms.

Because ATLID and CALIPSO are different instruments, their simulators are different, and are not expected to produce exactly the same clouds given the same atmosphere, even if part of the instrumental differences are taken into account within the simulators themselves. In the last part of this study, we compared the cloud observations simulated by COSP/ATLID and by COSP/CALIPSO for a given atmosphere predicted by LMDZ5 GCM. High cloud cover differences of 0.5% occur occasionally and rarely. Low cloud cover differences of 1% occur in midlatitudes. The ATLID-like cloud fraction profile is about 0.5% (1%) less than CALIPSO-like cloud fraction profile in daytime (nighttime): this difference mostly occur about 1 km in altitude below the maximum of the cloud fraction profile. The maximum relative difference between ATLID and CALIPSO height-SR histograms is respectively 0.5% and 1% in nighttime and daytime. The differences between ATLID-like and CALIPSO-like cloud fraction profiles are much lower than the differences between climate models + COSP/CALIPSO and CALIPSO observations that have been reported in CFMIP experiment [e.g., Konsta et al., 2012; Nam and Quaas, 2012; Kay et al., 2012; Nam et al., 2014; Bodas-Salcedo et al., 2014; Chepfer et al., 2014], suggesting that ATLID will provide useful observations to evaluate the cloud description in climate models, covering a time period complementary to the CALIPSO one. Moreover, at the time of writing, it is expected that ATLID will provide a better separation between boundary layer optically thin clouds and aerosols than CALIPSO does, thanks to ATLID new HSRL capability. Future work includes developing an ATLID GCM Climate Product from ATLID Level 1 data, following the same steps as for the COSP/ATLID simulator presented in this study; this product will include an advanced aerosol screening in the boundary layer using HSRL ATLID capability. This will facilitate comparisons between GCM + COSP/ATLID and ATLID GCM Climate Product to evaluate cloud descriptions in climate model.

Appendix A: Lidar Equation

At wavelengths of CALIOP (532 nm) and ATLID (355 nm), atmospheric cloud particles and gas molecules contribute to scattering but not to absorption except for ozone (ozone number densities and absorption cross section are provided in the CALIOP Level 1 data). The total attenuated backscatter (ATB) is then given by

$$ATB(\lambda, z) = [\beta_{part}(\lambda, z) + \beta_{mol}(\lambda, z)] \times \exp - 2 \int [\eta \times \alpha_{part}(\lambda, z) + \alpha_{mol}(\lambda, z)] dz \quad (A1)$$

where β_{part} and β_{mol} are lidar backscatter coefficients and α_{part} and α_{mol} are attenuation coefficients for particles (part) and molecules (mol), respectively, and η is the multiple-scattering coefficient, which has been approximated as a constant; otherwise, this parameter is function of range, particulate extinction, and viewing geometry.

Molecular backscatter and attenuation coefficients can be computed as a function of temperature and pressure [Collis and Russel, 1976]:

$$\beta_{\text{mol}}(\lambda, z) = \frac{P}{k_b T} \times 5.45 \times 10^{-32} \left(\frac{\lambda}{0.55} \right)^{-4.09} \quad (\text{A2})$$

$$\alpha_{\text{mol}}(\lambda, z) = \frac{8\pi}{3} \times \beta_{\text{mol}}(\lambda, z) \quad (\text{A3})$$

With P the pressure in Pa, T the temperature in K, k_b the Boltzmann constant, and λ the wavelength in μm . Assuming that the optical properties of atmospheric particles remain consistent along the lidar beam trajectory, and because at these wavelengths, attenuation by cloud particles (not aerosols) is only scattering, we can link particles backscatter and attenuation coefficients:

$$\beta_{\text{part}}(\lambda, z) = k_{\text{part}}(z) \times \alpha_{\text{part}}(\lambda, z) \quad (\text{A4})$$

$$\alpha_{\text{part}}(\lambda, z) = \int \pi r^2 Q(r) n(r, z) dr \quad (\text{A5})$$

with $k_{\text{part}}(z) = \frac{P(\pi)}{4\pi}$ the backscatter to extinction ratio when absorption is zero, r the particle radius, $n(r, z)$ the particle size distribution, $P(\pi)$ the backscattering phase function, and $Q(r)$ the scattering coefficient. For this study, we assume that the cloud particles are spherical; therefore, $P(\pi)$ is parameterized as a function of the effective radius using Mie theory (depending on the wavelength). Thus, most of the cloud particles are larger than the CALIOP and ATLID wavelengths so $Q(r)$ is set to 2 in equation (A5) [Bohren and Huffman, 1983].

The multiple scattering coefficient η theoretically varies between 0 and 1 for satellite lidar as a function of lidar footprint diameter and size, shape, and density of particles. For ground-based viewing geometry η can be less than zero [Platt, 1981]. The determination of this parameter is discussed in the main text.

Attenuated total molecular backscatter can be expressed as a function of molecular backscatter (equation (A2)) and attenuation coefficients (equation (A3)) :

$$\text{ATB}_{\text{mol}}(\lambda, z) = \beta_{\text{mol}}(\lambda, z) \times \exp \left[-2 \int \alpha_{\text{mol}}(\lambda, z) dz \right] \quad (\text{A6})$$

The scattering ratio is defined as the ration between the total attenuated backscatter (equation (A1)) over the molecular attenuated backscatter (equation (A6)):

$$\text{SR}(\lambda, z) = \frac{\text{ATB}(\lambda, z)}{\text{ATB}_{\text{mol}}(\lambda, z)} = \left[1 + \frac{\beta_{\text{part}}(\lambda, z)}{\beta_{\text{mol}}(\lambda, z)} \right] \times \exp \left[-2\eta(z) \int \alpha_{\text{part}}(\lambda, z) dz \right] \quad (\text{A7})$$

This ratio is equal to 1 in the absence of aerosol and cloud (pristine condition), is greater than 1 in presence of particles and/or aerosols, and in pristine air lying beneath a cloud or aerosol layer, this ratio is equal to the effective two-way transmittance of the overlying layer (i.e., it is less than 1).

It is important also to note that the signal-to-noise ratio of the scattering ratio is a function of the lidar wavelength as well as the signal-to-noise ratio of the signals themselves. This is an important issue to be aware of when comparing CALIPSO and ATLID scattering ratios. If, for simplicity, we neglect the particulate extinction, then applying standard error propagation techniques to equation (A7) we have

$$\text{SNR}_{\text{SR}_{532}} = \frac{\delta(\text{SR}_{532})}{\text{SR}_{532}} = \left(1 - \frac{1}{\text{SR}_{532}} \right) (\text{SNR}_{\text{ATB}_{532}})^{1/2} \quad (\text{A8})$$

where $\text{SNR}_{\text{ATB}_{532}}$ is the signal-to-noise ratio of the measured total attenuated backscatter. A similar expression for the scattering ratio SNR for ATLID (355 nm) can also be derived. Using the fact that $\beta_{\text{mol},355} \approx 5\beta_{\text{mol},532}$ it follows that $\text{SR}_{355} \approx \left(\frac{\text{SR}_{532}-1}{5} \right) + 1$ and

$$\frac{\text{SNR}_{\text{SR}_{532}}}{\text{SNR}_{\text{SR}_{355}}} \approx \frac{\left(1 - \frac{1}{\text{SR}_{532}} \right) (\text{SNR}_{\text{ATB}_{532}})^{1/2}}{\left(1 - \frac{1}{\left(\frac{\text{SR}_{532}-1}{5} \right) + 1} \right) (\text{SNR}_{\text{ATB}_{355}})^{1/2}} \quad (\text{A9})$$

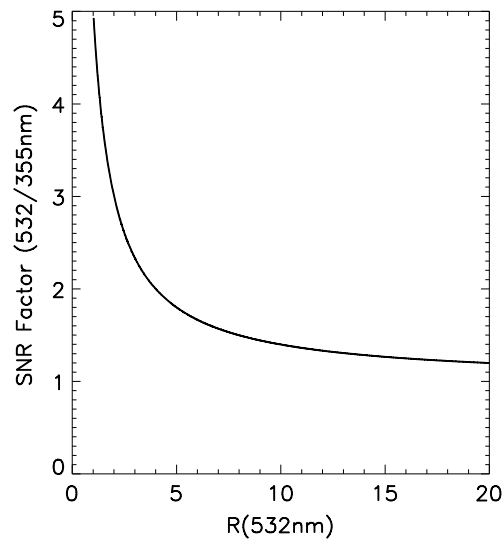


Figure A1. Ratio of the 532 to 355 nm scattering ratio signal-to-noise ratios as a function of scattering ratio at 532 nm calculated using equation (A10).

and if we assume (as is roughly true in the case of ATLID and CALIPSO) that the SNR of the measured attenuated backscatters is similar we have

$$\frac{\text{SNR}_{\text{SR}_{532}}}{\text{SNR}_{\text{SR}_{355}}} \approx \frac{\left(1 - \frac{1}{\text{SR}_{532}}\right)}{\left(1 - \frac{1}{\left(\frac{\text{SR}_{532}}{3} - 1\right) + 1}\right)} \quad (\text{A10})$$

A plot of equation (A10) is shown in Figure A1. Here it can be seen that for scattering ratios below about 5 that the green scattering ratios SNR values will be substantially above the corresponding 355 nm values. So for lidars with similar SNR ratios in terms of attenuated backscatter measurements, the SNR ratios associated with the scattering ratios are more favorable for 532 nm. This is a consequence of the much reduced amount of Rayleigh scattering at 532 nm compared to 355 nm. This difference has adverse consequences for the method used to detect clouds in this work.

Appendix B: Lidar Multiple-Scattering Calculations

In this appendix we describe the ECSIM lidar multiple-scattering model along with the its corresponding instrument model in more detail. We present additional examples of the application of ECSIM to CALIPSO simulations with the aim to support the realism of the simulation results.

B1. ECSIM Lidar Models

ECSIM is itself a modular software collection divided into scene-creation, forward radiative transfer, forward instrument models, and retrieval models. Consistent with this division, with respect to the lidar simulations, a two-step simulation procedure is applied. In particular, the spectrally and polarization resolved lidar signals as would be detected by a perfectly efficient lidar are calculated using a Monte Carlo approach. Then a separate instrument model is used to process the idealized signals taking into account factors such as the instrument polarization, noise, cross-talk and spectral responses associated with the different instrument channels along with their associated optical efficiencies. This approach allows one to easily change certain virtual instrument characteristics (e.g., detector efficiency) without having to re-run the potentially computationally expensive MC model.

The Monte Carlo model is similar to that described by *Hu et al.* [2001] but, in addition, can predict the spectral-polarization state of the lidar signal and employs a number of variance reduction techniques to increase the computational efficiency and is a true 3-D model, in which the cloud/aerosol fields can vary in both the

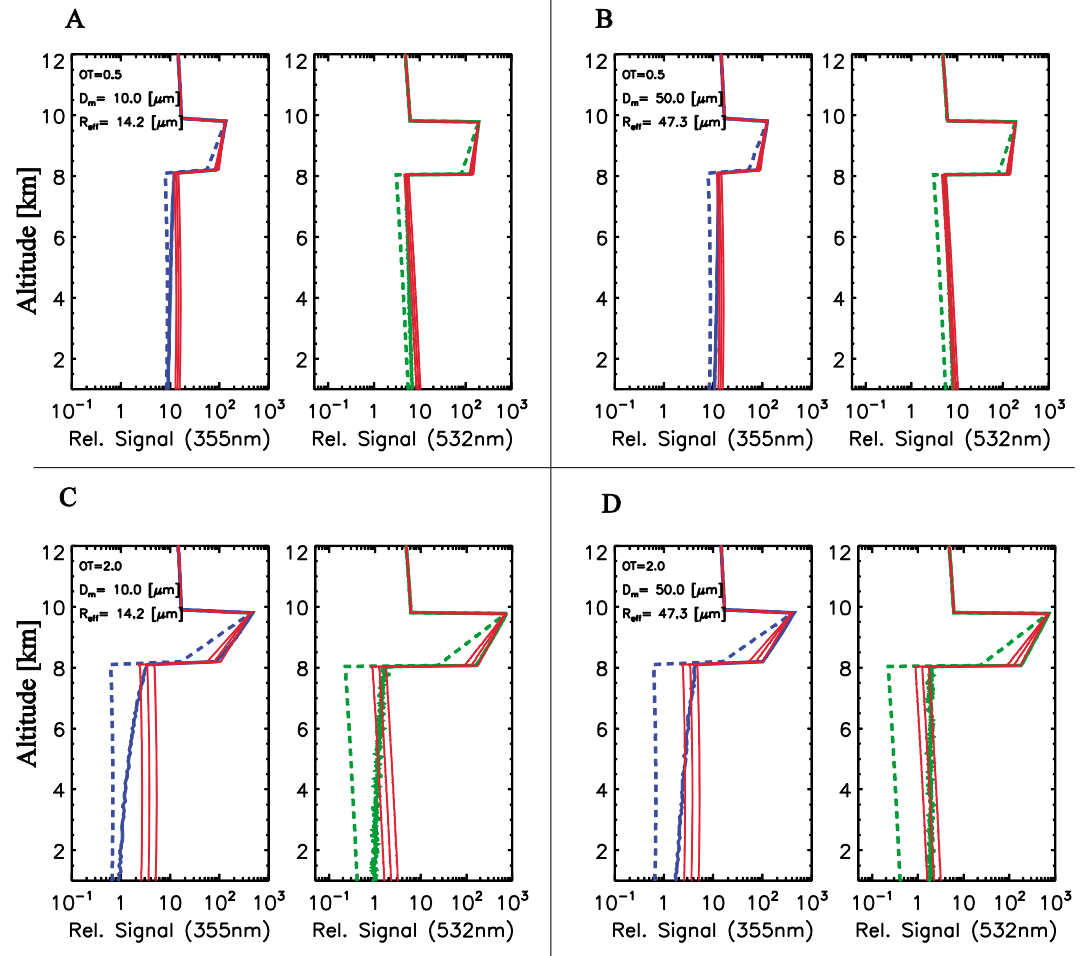


Figure B1. Example results of MC lidar radiative transfer simulations for ATLID (blue lines), CALIPSO (green lines) compared to the expected single-scatter signal levels (dotted Lines) and equation (A1) with $\eta = 0.4, 0.5$, and 0.6 (red-Lines). (a) $OT = 2$ and $D_m = 10.0 \mu\text{m}$. (b) Cirrus $OT = 2$, $D_m = 50.0 \mu\text{m}$ and $R_{\text{eff}} = 47.3 \mu\text{m}$. (c) Cirrus $OT = 0.5$, $D_m = 10.0 \mu\text{m}$. (d) Cirrus $OT = 0.5$, $D_m = 50.0 \mu\text{m}$ and $R_{\text{eff}} = 47.3 \mu\text{m}$.

vertical and horizontal directions. More detail regarding the ECSIM lidar Monte Carlo model may be found in Appendix A of *Donovan et al. [2015]*.

Noise is handled by first calculating the total number of photocounts per range bin (including lidar signal, signal corresponding to background scattered solar radiation, and instrument generated dark count rates) for each channel taking into account the channel characteristics. The background solar radiation is itself a function of surface albedo, solar zenith angle, and the effective atmospheric reflectance. Poissonian pseudo-random deviates are then used to generate the noisy signal profiles. Finally, background and darkcount signal levels are subtracted from the simulated signal profiles. SNR ratios of the signals generated by ECSIM compare favorably to typical nighttime and daytime CALIPSO observations. For example, for typical nighttime conditions, the observed SNR of the average value of 532 nm clear-air CALIPSO signals from 5 to 6 km are on the order of 80–100 for a 700 km horizontal averaging interval. For daytime conditions, the SNR for CALIPSO is less favorable ranging from 5 to 50 depending on the atmospheric state, surface reflectance, and solar zenith angle. For nighttime conditions ECSIM generates values that are generally consistent with CALIPSO observations within a factor of 20%. For daytime conditions, given the variability it is difficult to make a conclusive statement. However, it has been verified that for the examples presented in this paper that the daytime SNR ratios are consistent with the range expected from actual CALIPSO observations.

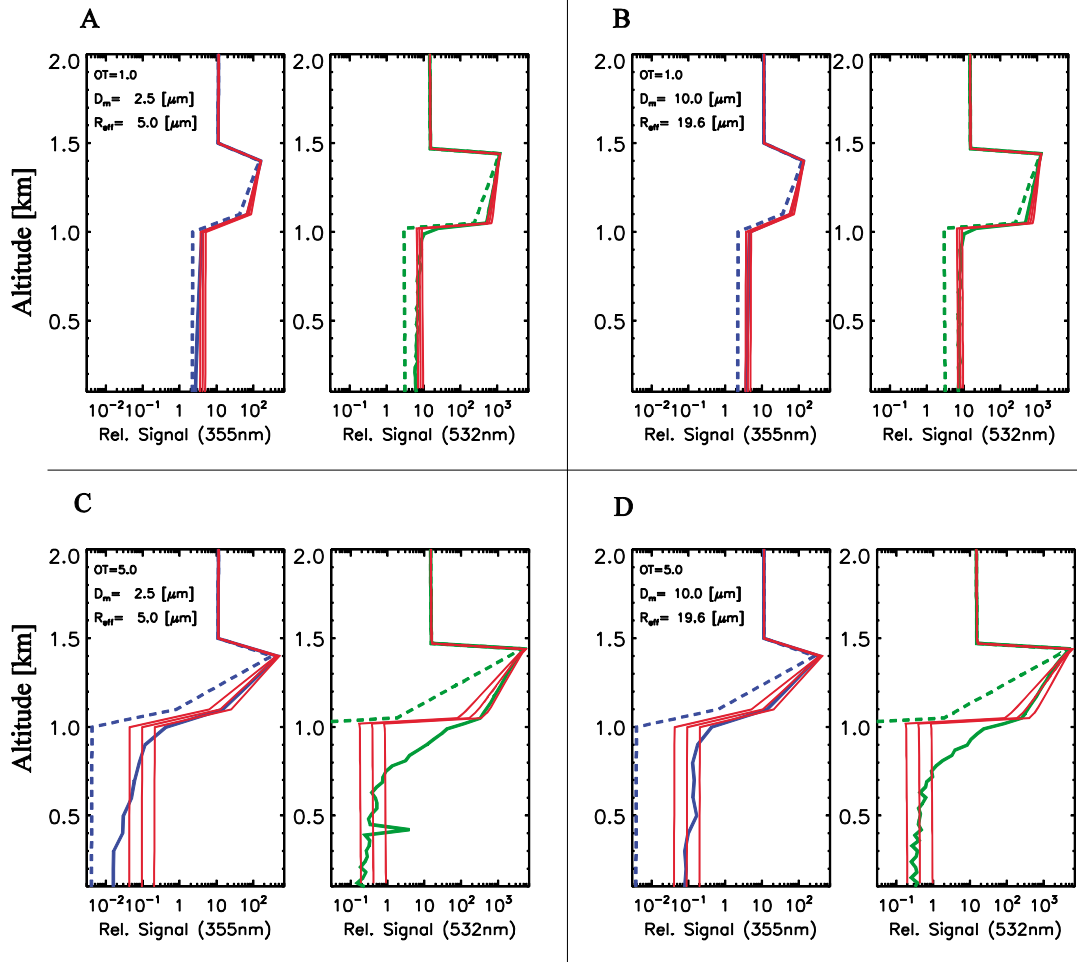


Figure B2. Example results of MC lidar radiative transfer simulations for ATLID (blue lines), CALIPSO (green lines) compared to the expected single-scatter signal levels for idealized water clouds (dotted Lines) and equation (A1) with $\eta = 0.4, 0.5$, and 0.6 (red-Lines) for the CALIPSO simulations while $\eta = 0.3, 0.4$, and 0.5 have been used for the ATLID simulations. The cloud optical thickness and particle sizes are as indicated in the plots. Spikes under the cloud are due to the statistical nature of the MC calculations and the small number of photon packets penetrating the cloud.

B2. Lidar MC Calculations

Results of sample MC calculations (without imposed instrument noise) are shown in Figure B1 for idealized cirrus clouds and Figure B2 for idealized water clouds. The phase functions used in the calculation are depicted (at 532 nm) in Figure B3. The cirrus phase function correspond to a gamma distribution of hexagonal crystals [Hess *et al.*, 1998a], while the water cloud phase functions correspond to gamma distributions [Hu and Stamnes, 1993] of cloud droplets; i.e.,

$$\frac{dN}{dr}(r) = \frac{N_0}{R_m} \frac{1}{\Gamma(\gamma)} \left(\frac{r}{R_m} \right)^{\gamma-1} \exp \left[-\frac{r}{R_m} \right]$$

where $D_m = 2R_m$ and for this type of distribution $R_{\text{eff}} = R_m(\gamma + 2)$.

An important factor in determining the characteristics of the MS lidar signal is the ratio of the forward scattering lobe to the lidar receiver field of view. The angular width of the forward scatter lobe decreases with increasing effective particle size. Thus, the cirrus phase functions are much more strongly peaked in the direct forward direction than the water cloud phase functions. The cloud optical depths at 532 and 355 nm are within a few percent of each other, and the corresponding phase functions at 355 nm (not shown) are only

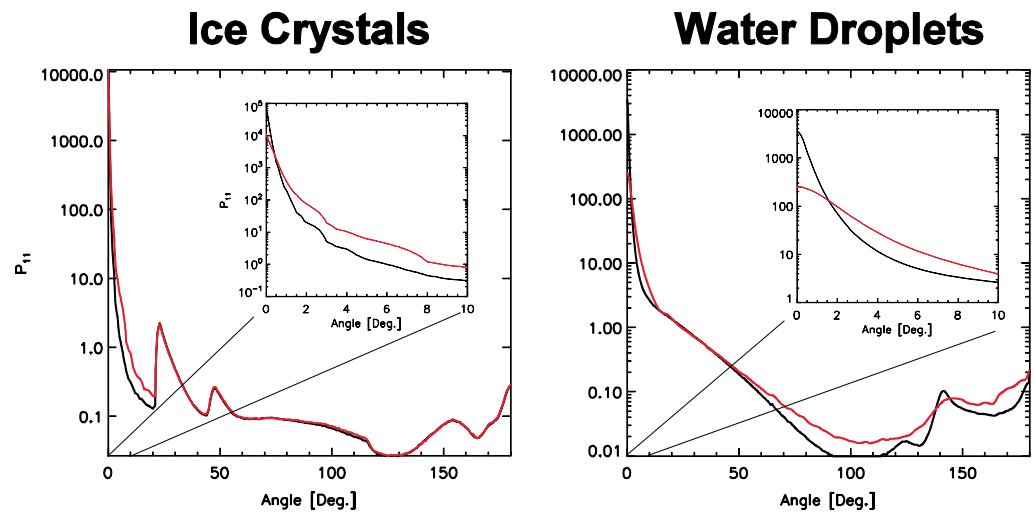


Figure B3. Phase functions at 532 nm for ice crystals used in the calculations for ice clouds shown in Figure B1 and for the water cloud simulations shown in Figure B2. The red lines in the left plot correspond to $D_m = 10 \mu\text{m}$, while the black line in the left plot correspond to $D_m = 50 \mu\text{m}$. In the right plot the red line corresponds to $D_m = 5.0 \mu\text{m}$, while the black line is for $D_m = 10.0 \mu\text{m}$.

somewhat more peaked than the 532 nm phase functions, and thus, the dominant difference between the MS signal characteristics between ATLID and CALIPSO are due to their respective fields of view.

Shown also in Figures B1 and B2 are the single-scattering signals as well as the signals predicted via the application of equation (A1) for different values of the MS coefficient as indicated in the figure captions. In general, it can be seen that equation (A1) performs well within the clouds; however, beneath cloud base the approach embodied by equation (A1) shows its limitation. In particular, for the ice cloud cases, for ATLID especially, a decay of the signal toward single-scatter values is apparent. For CALIPSO, this decay only becomes apparent for the high optical thickness and small particle case (Figure B2 (bottom left)). This behavior may be understood as follows:

1. Within the cloud the low mean-free path of the photons ensures that the multiple-scattered light tends to be confined to within the field of view of the lidar. However, the angular variance of the lidar beam will be broadened as it propagates downward through the cloud with more and more photons undergoing scattering events.
2. At cloud base the lidar beam emerges with an effective angular divergence, which increases with the optical thickness of the cloud and decreases with the size of the cloud particles (since the angular-width of the cloud phase function forward lobe increases with decreasing particle size).
3. Below cloud base the lidar beam will continue to propagate with a given divergence. However, the horizontal spread of the photons is no longer constrained by the presence of the cloud. As the beam continues to propagate downward, depending on the lidar receiver footprint, more and more of the multiple-scattered photons will travel outside of the receiver cone.
4. Since the effective footprint of CALIPSO is greater than that of ATLID the resulting decay below cloud base is much more noticeable for ATLID than CALIPSO. In fact, for CALIPSO, for the ice cloud cases shown, the decay length for CALIPSO is so long that it is only notable for relatively thick cirrus with relatively small particle sizes.

The decay effect is also a factor when attempting to calculate the ATB associated with multilayer cloud systems. Indeed, other simulations (not shown) applied to idealized multilayer cases, with low-level water clouds present below cirrus layers, show similar relative impacts on the water cloud ATB values as were observed with the cloud-free molecular below cloud returns.

For the water cloud examples the decay is apparent for both ATLID and CALIPSO for all the examples shown. This is due to the smaller (compared to the cirrus particles) size of the water cloud droplets and the resulting broader angular width of the forward scattering lobe.

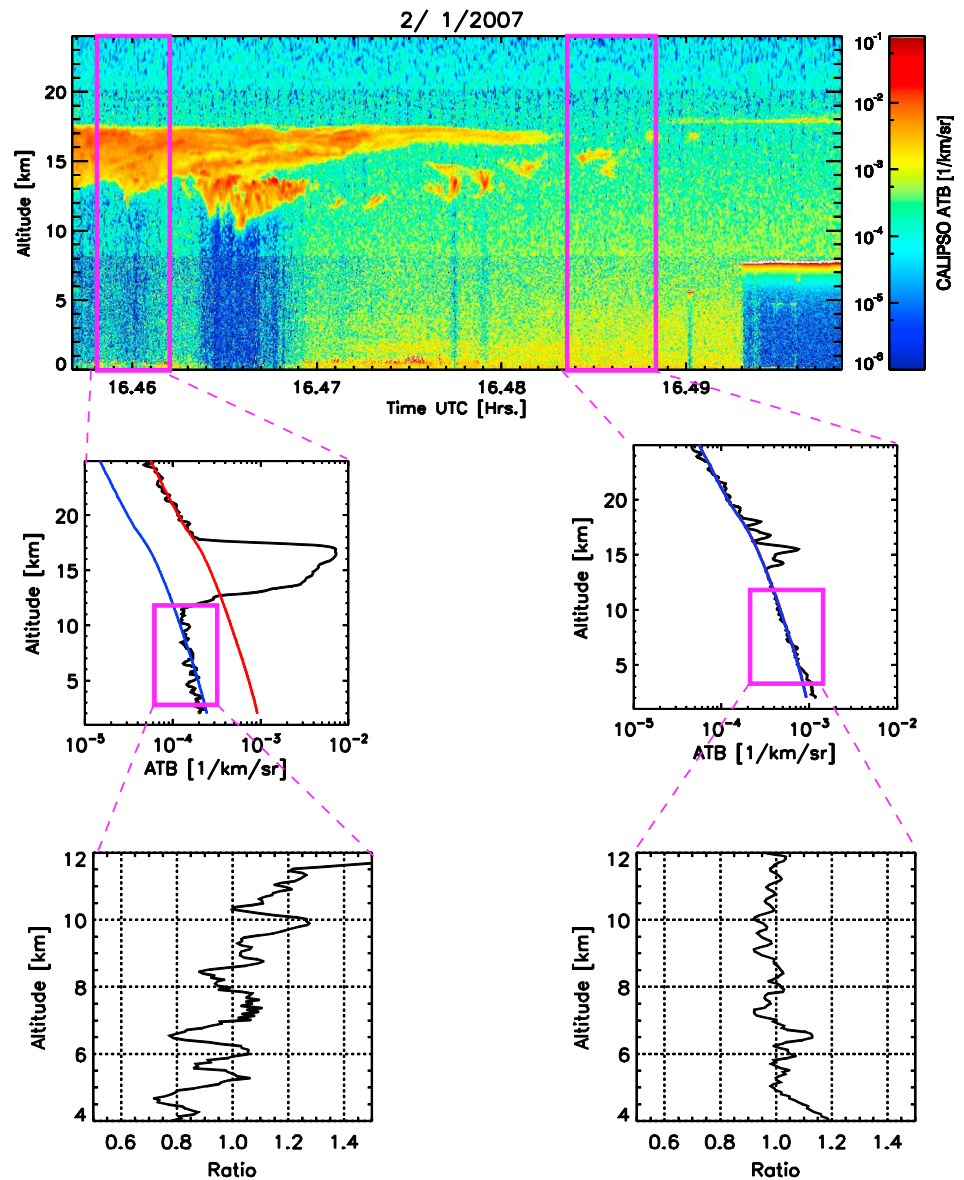


Figure B4. (top) CALIPSO attenuated backscatter from 16.48 to 16.5 UTC on 2 January 2007 (latitude/longitude from $-9.37, 137.7^{\circ}$ to $-10.29, 137.54^{\circ}$). (middle) Average profiles corresponding to the boxed regions shown in Figure B4 (top) along with theoretical cloud/aerosol-free attenuated backscatter profiles normalized to the observed average signals both below (blue) and above (red) the cloud layer (note in Figure B4, middle right); the red and blue curves overlap on this scale. (bottom) The respective ratios of the below-cloud observed attenuated backscatter profiles to the expected cloud/aerosol-free signal.

B3. CALIPSO MS Examples

Anecdotal, it has been noted by the authors of this work that it is not universally recognized that below cirrus multiple-scattering effects (the decay as predicted by our MS calculations) are present in CALIPSO signals. An extensive treatment of this issue is beyond the scope of this current work. However, here we present a representative case consistent with our calculations. An, by no means atypical, example of high tropical cirrus as measured by CALIPSO is shown in Figure B4. Here the left-highlighted cirrus cloud has a temperature in the range of -50°C to -70°C and thus is expected to be composed of crystals with effective radii on the regions of $10\text{--}20\text{ }\mu\text{m}$ [Donovan, 2003]. Further, by comparing the signal levels above and below the cloud it appears that the cloud is similar in optical thickness to the example shown in Figure B1 (bottom left). Thus, if our calculations are realistic, then a decay of the signal should be evident below the cloud base. In fact such a

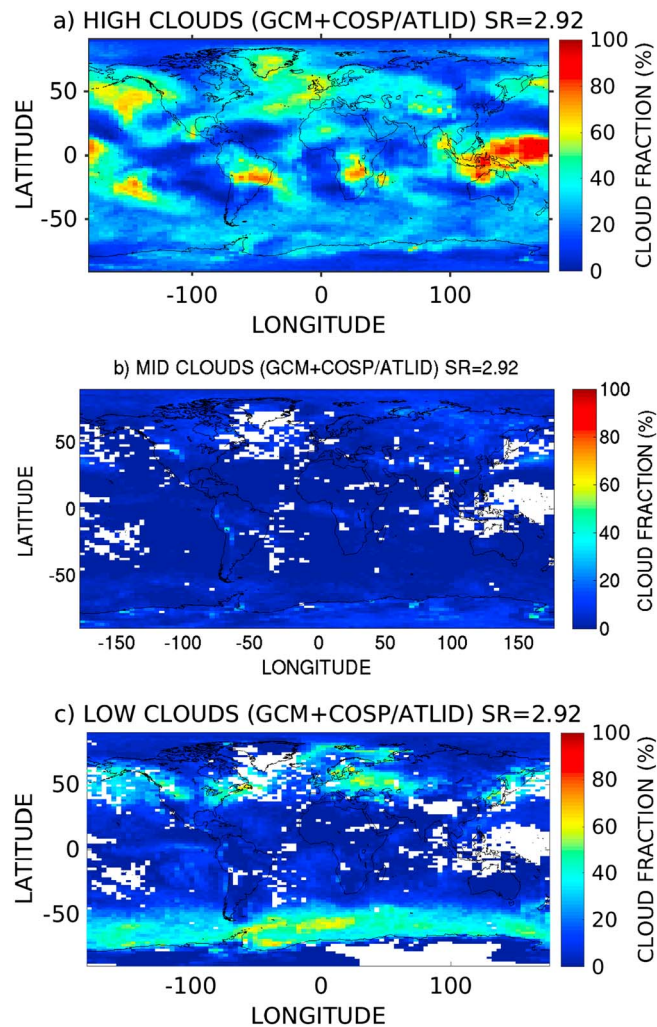


Figure C1. Cloud covers from GCM + COSP/ATLID in January. (a) High-level, (b) middle-level, and (c) low-level cloud covers. COSP/ATLID uses $\eta = 0.6$ and $SR_{DAY} = 2.92$. White pixels correspond to areas where the lidar signal is totally attenuated.

decay is indeed visible (see Figure B3, left) and (qualitatively) well matches our calculations in terms of magnitude and rate of decay. For comparison, average signals taken from a nearby region (right-highlighted area in Figure B4) with much thinner upper level cirrus show no such decay. The CALIOP 532 nm detectors are known to have a “nonideal transient response,” and after measuring a large signal they do not immediately recover, but instead shown an exponential decay [McGill *et al.*, 2007; Hunt *et al.*, 2009]. The $1/e$ time-constant associated with this nonideal response (on the order of 0.4–0.5 km or about 3.0 ms see, e.g., Figure 18 of Hunt *et al.* [2009]), however, is very fast compared with the decay time seen here. Thus, we feel that in this case the observed signal decay below the cirrus is primarily due to MS effects.

Appendix C: Global-Scale Clouds Simulated by COSP/ATLID

Figure C1 shows the low, middle, and high-level cloud maps obtained from LMDZ + COSP/ATLID. Unsurprisingly, the maps of high-level cloud cover ($z > 6.5$ km; Figure C1a) from COSP/ATLID simulator show the main expected cloud patterns: large clouds over the deep convective regions such as the warm pool, and in the continental Southern Hemisphere regions. The low cloud cover (Figure C1c) is small along the ITCZ because low-level clouds are masked by high optically thick clouds, through which the laser cannot pass. The low-level clouds are more numerous in the midlatitude storm tracks (50%), even if there are numerous high clouds above. The amount of midlevel clouds (Figure C1b) is very small as LMDZ GCM does not produce many.

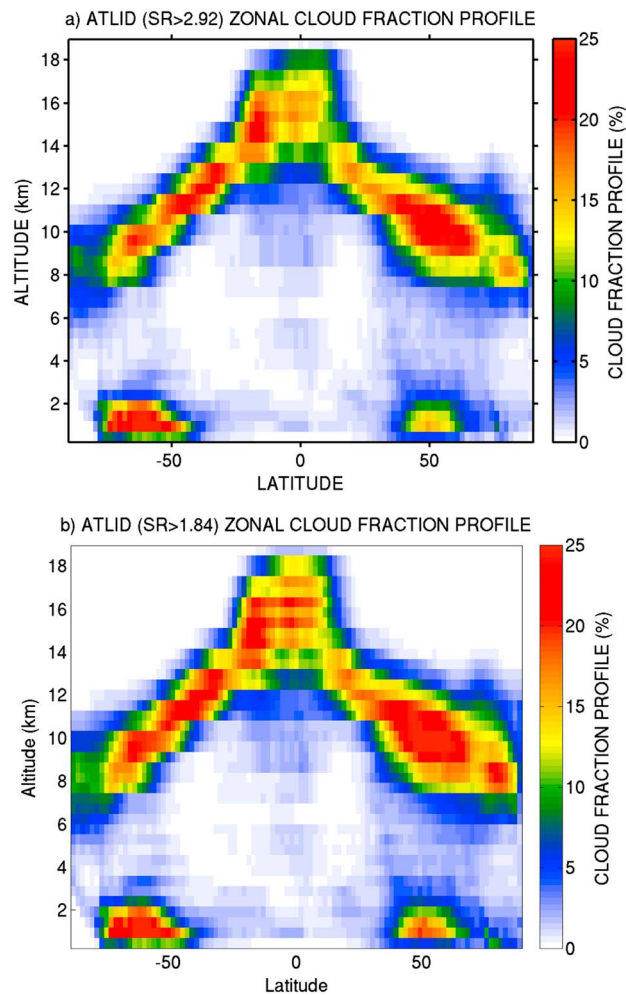


Figure C2. Zonal cloud fraction profile for GCM + COSP/ATLID in January. (a) In daytime COSP/ATLID uses $\eta = 0.6$ and $SR_{DAY} = 2.92$. (b) In nighttime, COSP/ATLID uses $\eta = 0.6$ and $SR_{NIGHT} = 1.84$.

Figure C2a shows zonal mean cloud fraction profiles from GCM + COSP/ATLID with the daytime cloud detection threshold: it shows the typical pattern of large-scale atmospheric circulation, with deep convective clouds along the ITCZ, the boundary layer clouds in the descend branch of the Hadley cell, and the storm tracks clouds in midlatitudes. Figure C2b shows the same as Figure C2a but using the nighttime cloud detection threshold. Figures C2a and C2b exhibit similar patterns but more clouds at high altitudes in the tropics and around 8 km of altitude in the Polar regions in nighttime, because the nighttime threshold detects more optically thin clouds than the daytime threshold. At midlatitude, more clouds are detected in the Northern Hemisphere with the nighttime threshold but not in the Southern Hemisphere. The imbalance between the Northern Hemisphere and the Southern Hemisphere suggests that this GCM produces more optically thin clouds ($1.84 < SR < 2.92$) in the Northern Hemisphere than in the Southern Hemisphere.

The height-intensity histogram (Figure C3) shows the number of detections in SR and height bins accumulated over different regions. Over the tropical western pacific area (Figure C3a), many large convective cloud systems are located between 14 km and 16 km with large SR and numerous fully attenuated profiles below 14 km of altitude. Few clouds are found between 4 and 8 km, and no clouds below 3 km, because the laser is fully attenuated in this region. Over the New Brunswick region (Figure C3b), cirrus clouds are simulated around 10 km, together with a significant amount of boundary layer clouds ($z < 3$ km) associated with large SR values. Over the North Pacific area (Figure C3), in the storms tracks, the frontal clouds with large vertical extent attenuate frequently the lidar signal below 10 km of altitude, but sparse boundary layer clouds are also detected.

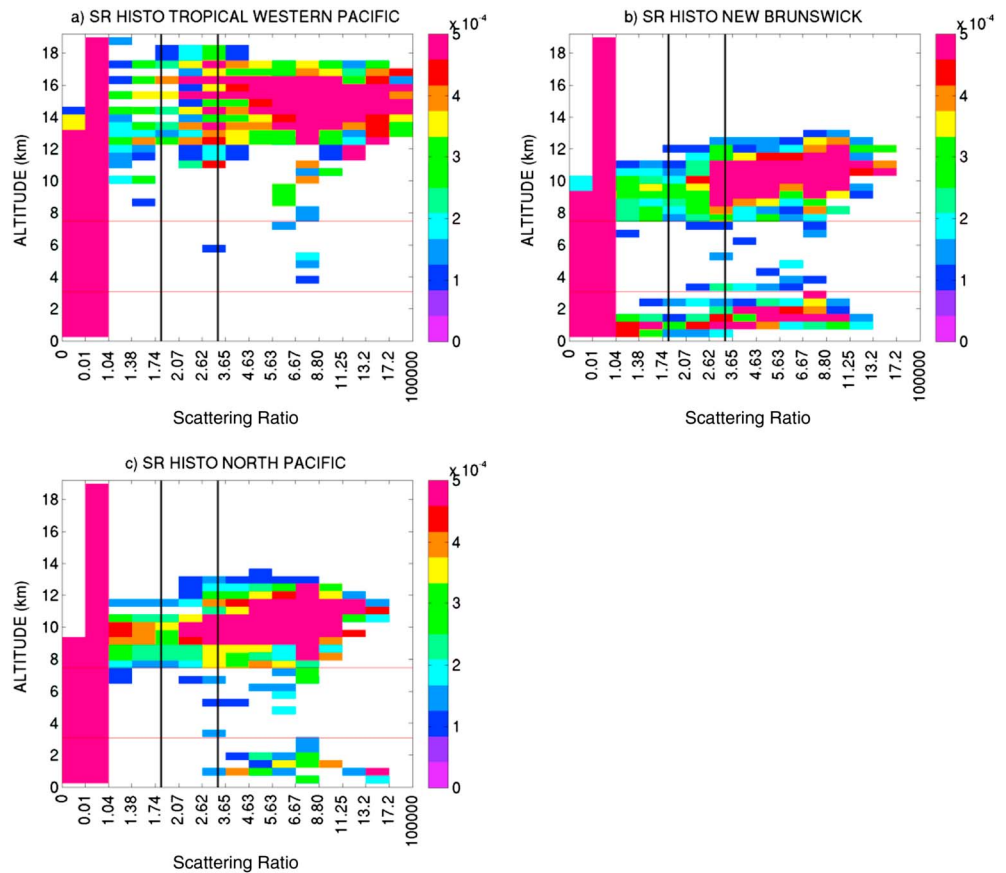


Figure C3. SR histogram from “GCM + COSP/ATLID” in January over (a) tropical Western Pacific, 70°E–150°E/5°S–20°N. (b) New Brunswick Region, 50°W–70°W/40°N–55°N. (c) North Pacific, 140°W–160°E/30°N–60°N. The horizontal axis show the ATLID SR bins. The black vertical lines correspond to $SR_{NIGHT} = 1.84$ and $SR_{DAY} = 2.92$ thresholds. The horizontal red lines separate low-, middle-, and high-level clouds.

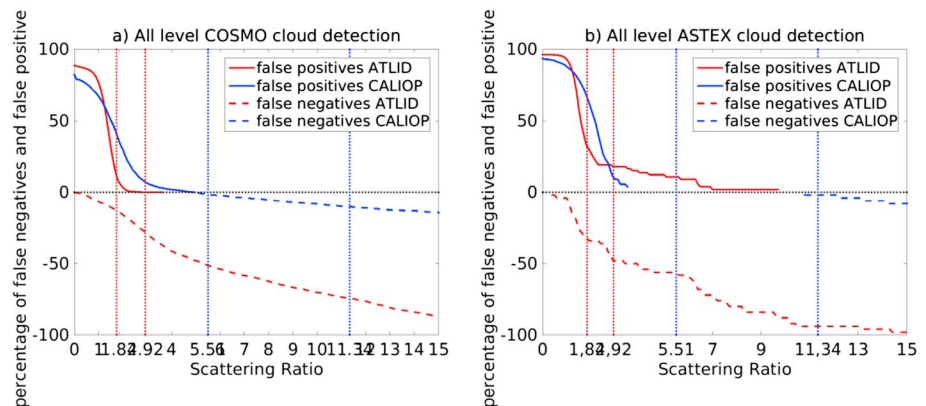


Figure C4. Percentage of false negatives cloud detections and false positives cloud detections as a function of the scattering ratio. The red (respectively blue) curve represents the ATLID detections (respectively CALIOP detections) for (a) COSMO case and (b) ASTEX case for different SR threshold values. Red vertical dotted lines represent the cloud day ($SR = 2.92$) and night ($SR = 1.84$) detection thresholds for ATLID. Blue vertical dotted lines represent the cloud day ($SR = 11.34$) and night ($SR = 5.51$) detection thresholds for CALIOP.

Acknowledgments

The authors acknowledge CNES and ESA for their contributions to fund this study. Thanks for NASA ASDC and ICARE/CGTD for access to CALIPSO data, and to the Climserv IPSL Computing Facilities for their support. CALIPSO-GOCCP data are available through <http://climserv.ipsl.polytechnique.fr/cfmip-obs/>, and COSP simulator data are available through <http://cfmip.metoffice.com/COSP.html>. ECSIM is distributed at ESA/ESTEC. The other data used in this paper (MC simulations and GCM + COSP/ATLID) are available upon request. They thank all anonymous reviewers for useful comments and feedback.

References

- Bodas-Salcedo, A., et al. (2011), COSP: Satellite simulation software for model assessment, *Bull. Am. Meteorol. Soc.*, 92, 1023–1043, doi:10.1175/2011BAMS2856.1.
- Bodas-Salcedo, A., K. D. Williams, M. A. Ringer, I. Beau, J. N. S. Cole, J.-L. Dufresne, T. Koshiro, B. Stevens, Z. Wang, and T. Yokohata (2014), Origins of the solar radiation biases over the Southern Ocean in CFMIP2 models*, *J. Clim.*, 27, 41–56, doi:10.1175/JCLI-D-13-00169.1.
- Bohren, C. F., and D. R. Huffman (1983), *Absorption and Scattering of Light by Small Particles*, Wiley, Weinheim, Germany, doi:10.1002/9783527618156.
- Bony, S., M. Webb, B. Stevens, C. Bretherton, S. Klein, and G. Tselioudis (2009), The Cloud Feedback Model Intercomparison Project: Summary of activities and recommendations for advancing assessments of cloud-climate feedbacks.
- Intergovernmental Panel on Climate Change (2013), *Climate Change 2013: The Physical Science Basis. Contribution of Working Group I to the Fifth Assessment Report of the Intergovernmental Panel on Climate Change*, edited by T. F. Stocker et al., 1535 pp., Cambridge Univ. Press, Cambridge, U. K., and New York.
- Bucholtz, A. (1995), Rayleigh-scattering calculations for the terrestrial atmosphere, *Appl. Opt.*, 34, 2765–2773, doi:10.1364/AO.34.002765.
- Cesana, G., and H. Chepfer (2013), Evaluation of the cloud water phase in a climate model using CALIPSO-GOCCP, *J. Geophys. Res. Atmos.*, 118, 7922–7937, doi:10.1002/jgrd.50376.
- Chepfer, H., M. Chiriaco, R. Vautard, and J. Spinhirne (2007), Evaluation of MM5 optically thin clouds over Europe in fall using ICESat lidar spaceborne observations, *Mon. Weather Rev.*, 135, 2737–2753, doi:10.1175/MWR3413.1.
- Chepfer, H., S. Bony, D. Winker, M. Chiriaco, J.-L. Dufresne, and G. Seze (2008), Use of CALIPSO lidar observations to evaluate the cloudiness simulated by a climate model, *Geophys. Res. Lett.*, 35, L15704, doi:10.1029/2008GL034207.
- Chepfer, H., S. Bony, D. Winker, G. Cesana, J. L. Dufresne, P. Minnis, C. J. Stubenrauch, and S. Zeng (2010), The GCM-Oriented CALIPSO Cloud Product (CALIPSO-GOCCP), *J. Geophys. Res.*, 115, D00H16, doi:10.1029/2009JD012251.
- Chepfer, H., G. Cesana, D. Winker, B. Getzewich, and M. Vaughan (2013), Comparison of two different cloud climatologies derived from CALIOP Level 1 observations: the CALIPSO-ST and the CALIPSO-GOCCP, *J. Atmos. Oceanic Technol.*, doi:10.1175/JTECH-D-12-00057.1.
- Chepfer, H., V. Noel, D. Winker, and M. Chiriaco (2014), Where and when will we observe cloud changes due to climate warning?, *Geophys. Res. Lett.*, 41, 8387–8395, doi:10.1002/2014GL061792.
- Chiriaco, M., R. Vautard, H. Chepfer, M. Haeffelin, J. Dudhia, Y. Wanherdrick, Y. Morille, and A. Protat (2006), The ability of MM5 to simulate ice clouds: Systematic comparison between simulated and measured fluxes and lidar/radar profiles at the SIRT Atmospheric Observatory, *Mon. Weather Rev.*, 134, 897–918, doi:10.1175/MWR3102.1.
- Collis, R. T. A., and P. B. Russel (1976), *Laser Monitoring of the Atmosphere*, pp. 108, Springer, New York.
- Donovan, D. P. (2003), Ice-cloud effective particle size parameterization based on combined lidar, radar reflectivity, and mean Doppler velocity measurements, *J. Geophys. Res.*, 108, 2156–220, doi:10.1029/2003JD003469.
- Donovan, D. P., R. H. Voors, G. J. van Zadelhoff, and J. R. Acaretta (2008), ECSIM model and algorithms document external project, Technical Report EarthCARE Simulator. [Available at: <http://www.knmi.nl/~zadelhof/file/ECSIM-KNMI-TEC-MAD01-122-R.pdf>.]
- Donovan, D. P., H. Klein Baltink, J. S. Henzing, S. R. de Roode, and A. P. Siebesma (2015), A depolarisation lidar-based method for the determination of liquid-cloud microphysical properties, *Atmos. Meas. Tech.*, 8, 237–266, doi:10.5194/amt-8-237-2015.
- Durand, Y., A. Hélière, J.-L. Bézy, and R. Meynart (2007), The ESA EarthCARE mission: Results of the ATLID instrument pre-developments, *Proc. SPIE*, 6750, 675015, doi:10.1117/12.737932.
- Eloranta, E. W. (1972), Calculation of doubly scattered lidar returns, PhD thesis, Univ. of Wisconsin-Madison, Dep. of Meteorology.
- Francis, P. N., A. Jones, R. W. Saunders, K. P. Shine, A. Slingo, and Z. Sun (1994), An observational and theoretical study of the radiative properties of cirrus: Some results from ICE'89, *Q. J. R. Meteorol. Soc.*, 120, 809–848, doi:10.1002/qj.49712051804.
- Hagihara, Y., H. Okamoto, and R. Yoshida (2010), Development of a combined CloudSat-CALIPSO cloud mask to show global cloud distribution, *J. Geophys. Res.*, 115, D00H33, doi:10.1029/2009JD012344.
- Hélière, A., R. Gelsthorpe, L. Le Hors, and Y. Toulemont (2012), ATLID, the atmospheric lidar on board the EarthCARE satellite, International conference on space optics, October 2012, France.
- Hess, M., R. B. A. Koelmeyer, and P. Stammes (1998a), Scattering matrices of imperfect hexagonal ice crystals, *J. Quant. Spectrosc. Radiat. Transfer*, 60, 301–308.
- Hess, M., P. Koepke, and I. Schult (1998b), Optical properties of aerosols and clouds: The software package OPAC, *Bull. Am. Meteorol. Soc.*, 79, 831–844.
- Hogan, R. (2006), Fast, approximate calculation of multiply scattered lidar returns, *Appl. Opt.*, 45, 5984–5992, doi:10.1364/AO.45.005984.
- Hourdin, F. J.-Y., et al. (2013), LMDZ5B: The atmospheric component of the IPSL climate model with revisited parameterizations for clouds and convection, *Clim. Dyn.*, 40, 2193–2222.
- Hu, Y., et al. (2001), Identification of cloud phase from PICASSO-CENA lidar depolarization: A multiple scattering sensitivity study, *J. Quant. Spectrosc. Radiat. Transfer*, 70, 569–579.
- Hu, Y.-X., and K. Stamnes (1993), An accurate parameterization of the radiative properties of water clouds suitable for use in climate models, *J. Clim.*, 6(4), 728–742.
- Hunt, W. H., D. M. Winker, M. A. Vaughan, K. A. Powell, P. L. Luckner, and C. Weimer (2009), CALIPSO lidar description and performance assessment, *J. Atmos. Oceanic Technol.*, 26, 1214–1228, doi:10.1175/2009JTECHA1223.1.
- Illingworth, A. J., et al. (2014), THE EARTH CARE SATELLITE: The next step forward in global measurements of clouds, aerosols, precipitation and radiation, *Bull. Am. Meteorol. Soc.*, 96, 1311–1332, doi:10.1175/BAMS-D-12-00227.1.
- Kato, S., et al. (2011), Improvements of top-of-atmosphere and surface irradiance computations with CALIPSO-, CloudSat-, and MODIS-derived cloud and aerosol properties, *J. Geophys. Res.*, 116, D19209, doi:10.1029/2011JD016050.
- Kay, J. E., et al. (2012), Exposing global cloud biases in the Community Atmosphere Model (CAM) using satellite observations and their corresponding instrument simulators, *J. Clim.*, 25, 5190–5207, doi:10.1175/JCLI-D-11-00469.1.
- Konsta, D., H. Chepfer, and J. L. Dufresne (2012), A process oriented description of tropical oceanic clouds for climate model evaluation, based on a statistical analysis of daytime A-train high spatial resolution observations, *Clim. Dyn.*, doi:10.1007/s00382-012-1533-7.
- L'Ecuyer, T. S., N. Wood, T. Haladay, and G. L. Stephens (2008), The impact of clouds on atmospheric heating based on the R04 CloudSat fluxes and heating rate dataset, *J. Geophys. Res.*, 113, D00A15, doi:10.1029/2008JD009951.
- Marchand, R. T., J. Haynes, G. G. Mace, T. Ackerman, and G. Stephens (2009), A comparison of simulated cloud radar output from the multiscale modeling framework global climate model with CloudSat cloud radar observations, *J. Geophys. Res.*, 114, D00A20, doi:10.1029/2008JD009790.
- McGill, M. J., M. A. Vaughan, C. R. Trepte, W. D. Hart, D. L. Hlavka, D. M. Winker, and R. Kuehn (2007), Airborne validation of spatial properties measured by the CALIPSO lidar, *J. Geophys. Res.*, 112, D20201, doi:10.1029/2007JD008768.

- Nam, C. C. W., and J. Quaas (2012), Evaluation of clouds and precipitation in the ECHAM5 general circulation model using CALIPSO and CloudSat satellite data, *J. Clim.*, *25*, 4975–4992, doi:10.1175/JCLI-D-11-00347.1.
- Nam, C., J. Quaas, R. Neggers, C. Siegenthaler-Le Drian, and F. Isotta (2014), Evaluation of boundary layer cloud parameterizations in the ECHAM5 general circulation model using CALIPSO and CloudSat satellite data, *J. Adv. Model. Earth Syst.*, *6*, 300–314, doi:10.1002/2013MS000277.
- Noel, V., H. Chepfer, G. Ledanois, A. Delaval, and P. Flamant (2002), Classification of particle shape ratios in cirrus clouds based on the lidar depolarization ratio, *Appl. Opt.*, *41*, 4245–4257, doi:10.1364/AO.41.004245.
- Noel, V., H. Chepfer, C. Hoareau, M. Reverdy, and G. Cesana (2014), Effect of solar activity and geomagnetic field on noise in CALIOP profiles above South Atlantic Anomaly, *Atmos. Meas. Tech.*, doi:10.5194/amt-7-1597-2014.
- Petzold, A., et al. (2011), Inter-comparison of aerosol retrievals and observational requirements for multi-wavelength HSRL systems, Final report, ESA/ESTEC contract 22169/NL/CT, Tech. Rep. ESA-ESTEC (European Space Agency).
- Placidi, S., F. Faure, D. P. Donovan, B. Mayer, R. Buras, and H. W. J. Russchenberg (2010), Comparison of two distinct EarthCARE multi spectral imager simulators, EUMETSAT Meteorological Satellite Conference, online, pp. 1–7, Córdoba, Spain, 20–24 Sept.
- Platt, C. (1973), Lidar and Radiometric observations of cirrus clouds, *J. Atmos. Sci.*, *30*, 1191–1204.
- Platt, C. M. R. (1981), Remote sounding of High Clouds. III: Monte Carlo calculations of multiple-scattered lidar returns, *J. Atmos. Sci.*, *38*, 156–167.
- Randall, D. A., et al. (2007), Climate models and their evaluation, in *Climate Change 2007: The Physical Science Basis. Contribution of Working Group I to the Fourth Assessment Report of the Intergovernmental Panel on Climate Change*, edited by S. Solomon et al., Cambridge Univ. Press, Cambridge, U. K., and New York.
- Spinhirne, J. D., S. P. Palm, W. D. Hart, D. L. Hlavka, and E. J. Welton (2005), Cloud and aerosol measurements from GLAS: Overview and initial results, *Geophys. Res. Lett.*, *32*, L22S03, doi:10.1029/2005GL023507.
- Stephens, G. L., et al. (2002), The CloudSat mission and the A-Train: A new dimension of space-based observations of clouds and precipitation, *Bull. Am. Meteorol. Soc.*, *83*, 1771–1790, doi:10.1175/BAMS-83-12-1771.
- Stubenrauch, C. J., et al. (2013), Assessment of global cloud datasets from satellites: Project and database initiated by the GEWEX radiation panel, *Bull. Am. Meteorol. Soc.*, doi:10.1175/BAMS-D-12-00117.
- Vaughan, M. A., K. A. Powell, R. E. Kuehn, S. A. Young, D. M. Winker, C. A. Hostetler, W. H. Hunt, Z. Liu, M. J. McGill, and B. J. Getzewich (2009), Fully automated detection of cloud and aerosol layers in the CALIPSO lidar measurements, *J. Atmos. Oceanic Technol.*, *26*, 2034–2050, doi:10.1175/2009JTECHA1228.1.
- Voors, R., D. P. Donovan, J. Acarreta, M. Eisinger, R. Franco, D. Lajas, R. Moyano, F. Pirondini, and J. T. Wehr (2007), ECSIM: The simulator framework for EarthCARE, *Proc. SPIE 6744, Sensors, Systems, and Next-Generation Satellites XI*, 67441Y (October 17, 2007), doi:10.1117/12.737738.
- Winker, D. M., et al. (2010), The CALIPSO mission: A global 3D view of aerosols and clouds, *Bull. Am. Meteorol. Soc.*, *91*, 1211–1229, doi:10.1175/2010BAMS3009.1.
- Winker, D., R. H. Couch, and M. P. McCormick (1996), An overview of LITE: NASA's lidar in-space technology experiment, *Proc. IEEE*, *84*, 2, 164–180.
- Winker, D., W. Hunt, and M. McGill (2007), Initial performance assessment of CALIOP, *Geophys. Res. Lett.*, *34*, L19803, doi:10.1029/2007GL030135.